The Role of Momentum Transport in the Motion of a Quasi-Idealized Mesoscale Convective System

KELLY M. MAHONEY, GARY M. LACKMANN, AND MATTHEW D. PARKER

Department of Marine, Earth, and Atmospheric Sciences, North Carolina State University, Raleigh, North Carolina

(Manuscript received 1 December 2008, in final form 26 April 2009)

ABSTRACT

Momentum transport is examined in a simulated midlatitude mesoscale convective system (MCS) to investigate its contribution to MCS motion. Momentum budgets are computed using model output to quantify the role of specific processes in determining the low-level wind field in the system's surface-based cold pool. Results show that toward the leading convective line of the MCS and near the leading edge of the cold pool, the momentum field is most strongly determined by the vertical advection of the storm-induced perturbation wind. Across the middle rear of the system, the wind field is largely a product of the pressure gradient acceleration and, to a lesser extent, the vertical advection of the background environmental (i.e., base state) wind. The relative magnitudes of the vertical advection terms in an Eulerian momentum budget suggest that, for gust-front-driven systems, downward momentum transport by the MCS is a significant driver of MCS motion and potentially severe surface winds. Results further illustrate that the contribution of momentum transport to MCS speed occurs mainly via the enhancement of the cold pool propagation speed as higher-momentum air from aloft is transported into the surface-based cold pool.

1. Introduction

The study of mesoscale convective systems (MCSs) is motivated by an array of theoretical questions regarding their formation, movement, and dynamics, and also by the high-impact weather that these complex systems often produce. MCS motion is often the combined result of several physical processes that occur on different temporal and spatial scales; its prognostication remains a challenge to human forecasters and numerical weather prediction (NWP) models alike (e.g., Corfidi 2003). A large body of past research has explored various mechanisms by which these systems move (e.g., cold pools and gravity waves), and the goal of this investigation is an in-depth assessment of a process that may also significantly affect MCS motion: the transport and adjustment of momentum within an MCS.

Figure 1 conceptually illustrates aspects of the convective momentum transport (CMT) process, using an adaptation of the Houze et al. (1989) classic leading-convective, trailing-stratiform MCS archetype. This illustration shows how flow from the rear of the system is accelerated via the pressure gradient force and transported downward, the strongest winds forming the rear-inflow jet (RIJ; e.g., Smull and Houze 1987). The degree to which the combined momentum of the environmental and storm-induced wind fields is transported downward depends on a number of factors including the strength of the RIJ and the magnitude of negative buoyancy in the trailing-stratiform region (e.g., Houze et al. 1989; Lafore and Moncrieff 1989), as well as downdrafts and/or negative buoyancy generated in the convective region (e.g., Zipser 1977; Klimowski 1994). The extent to which the RIJ descends relative to the surface has implications for MCS motion as well as the potential for damaging winds. Weisman (1992) detailed how this process may be determined by the resulting vorticity balance between the convective and stratiform MCS regions, and recent research by Trapp and Weisman (2003) and Atkins and St. Laurent (2009) finds that a descending RIJ may cause severe surface winds when collocated with a mesovortex along the leading convective line. The MCS momentum field is ultimately the combined effect of the processes described above, in addition to contributions imparted by both the larger-scale flow (e.g., Smull and Houze 1987) as well as convective-scale transports of varying magnitude occurring throughout the storm (e.g., Yuter

Corresponding author address: Kelly Mahoney, Department of Marine, Earth, and Atmospheric Sciences, North Carolina State University, Raleigh, NC 27695.
E-mail: kmmahon2@ncsu.edu

DOI: 10.1175/2009MWR2895.1

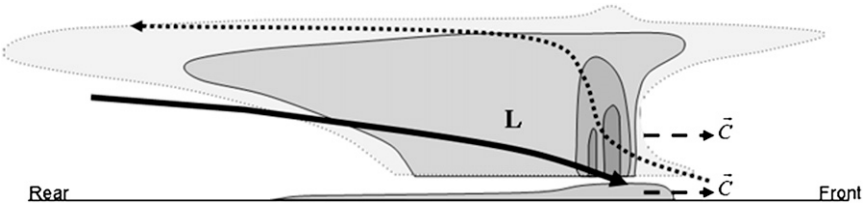

FIG. 1. Schematic of hypothesized momentum transport mechanism in an idealized MCS. Based on Houze et al. (1989), where outermost dotted outline represents cloud outline, inner shaded solid contours represent radar reflectivity, and shaded area at surface represents the cold pool. Boldface "L" denotes approximate area of midlevel mesolow; thick downward-sloping arrow shows rear-to-front flow, and dashed upward-sloping arrow shows front-to-rear flow branch. Dashed arrow denotes **C**, the accelerated speed at which the cold pool and MCS move.

and Houze 1995; Bryan et al. 2003). Thus, CMT is defined herein as the total momentum adjustment that results from the presence of an MCS. That is, the term includes both mesoscale and convective-scale adjustments, and refers to all changes realized in the momentum field, including those due to both acceleration and transport.

The overarching goal of this investigation is to improve understanding of the processes that drive MCS motion, especially CMT. Enhanced insight into these processes will help to improve severe weather forecasting and potentially increase warning times for phenomena such as straight-line wind damage—an issue of critical concern when strong rear inflow descends to the surface (e.g., Johns and Hirt 1987; Weisman 1992; Wakimoto et al. 2006). A secondary motivation for this work stems from the neglect of CMT in some convective parameterization (CP) schemes. One shortcoming of some CP schemes [e.g., operational implementations of the Betts–Miller–Janjić (Betts 1986; Janjić 1994), Kain–Fritsch (Kain and Fritsch 1993), and Grell (Grell 1993) schemes] is the omission or oversimplification of momentum adjustment[1]—we hypothesize that this may sometimes inhibit accurate representation of MCS motion in operational model forecasts. This limitation has also been suggested by previous research demonstrating that NWP model forecasts of an observed MCS in which a CP scheme is employed exhibited a negative bias in forecast MCS speed (Mahoney and Lackmann 2007). Convective parameterization schemes are challenged on both the meso- and convective scales to accurately represent MCS motion. For example, Correia et al. (2008) found a distorted RIJ (generally a mesoscale feature) resulting from the use of a CP scheme, and many past studies caution against the omission of critical convective-scale processes (e.g., convective downdrafts and turbulent mixing) resulting from the use of larger grid spacings and CP schemes (e.g., Weisman et al. 1997; Bryan et al. 2003). Therefore, while there exist many challenges to successful numerical simulations of MCSs (e.g., correct representation of the vertical heating profile; Pandya and Durran 1996; Correia et al. 2008), neglecting or poorly resolving CMT within an MCS is likely detrimental to MCS motion forecasts from both the meso- and convective-scale perspectives. Thus, though we define CMT herein to include both scales of motion, differentiating the two for CP scheme applications is an avenue of future research. While increased computing power may eventually render CP schemes unnecessary for short- and medium-range operational forecasting, they will likely remain essential for climate models and global ensemble forecasts; therefore, improving such schemes will remain a valuable contribution, even after mesoscale operational models are run without them.

MCS motion comprises an advective component $\mathbf{C}_A$ and a propagative component $\mathbf{C}_P$, where the motion of the MCS ($\mathbf{C}$) is the sum of these two components, $\mathbf{C} = \mathbf{C}_A + \mathbf{C}_P$ (e.g., Newton and Newton 1959; Bluestein and Jain 1985; Corfidi et al. 1996; Fritsch and Forbes 2001). The advective component of motion is generally determined by the mean cloud-bearing wind (e.g., Newton and Newton 1959; Corfidi et al. 1996), whereas propagation may be continuous (e.g., driven by the continual spreading of the subcloud cold pool) or discrete (forming ahead of an existing gust front, e.g., Fovell et al. 2006). Many questions remain as to why observed MCSs assume a given speed or direction of motion, as well as which physical processes dominate in a given background environment (e.g., Houze 2004). The present paper asks the question: In what ways does CMT affect MCS motion? The findings described herein provide a

[1] The treatment of momentum adjustment varies widely in different CP schemes, from complete omission to more sophisticated schemes based on perturbation pressure gradient relationships (e.g., Wu and Yanai 1994; Carr and Bretherton 2001; Han and Pan 2006; Moncrieff and Liu 2006; Hogan and Pauley 2007; Wu et al. 2007).

unique contribution to the study of MCS motion by describing a process that (to the authors' knowledge) has not been thoroughly examined as it specifically relates to MCS motion. This paper further examines whether changes in MCS speed are primarily due to the advective component of system motion (i.e., system speed changes as a result of changes in the mean cloud-bearing wind), or to the propagative component (i.e., altering cold pool characteristics, thereby affecting new cell growth and thus system speed). We begin by describing CMT and its treatment in previous studies, and then quantify the process in a numerically simulated MCS to examine its effect on system motion.

2. Background

a. Previous related research

Past studies have examined CMT within MCSs, but most have focused on its effect on the large-scale momentum field of the surrounding environment, or its parameterization in large-scale numerical models (e.g., Houze 1973; Grubišić and Moncrieff 2000; Mechem et al. 2006). Recent studies by Houze et al. (2000) and Mechem et al. (2006) have advanced the idea that momentum transport within and beneath the stratiform region of tropical MCSs can significantly impact the lower-tropospheric wind field. One of the two main regimes studied by Mechem et al. (2006) examines the enhancement of surface westerly winds via the downward transport of upper-level westerly momentum. While their findings focus on the effect of this transport on the large-scale momentum field, it follows that such a feedback might also impact the translational speed of the MCS by changing the wind within the cold pool. Here, we wish to examine the effect of this latter aspect, distinct from that of most previous studies: What influence does the vertical momentum transport (of both large-scale and perturbation winds) by an MCS have on the ground speed of the MCS itself?

Many previous studies that have examined CMT in MCSs have employed intricate momentum budgets (e.g., Sanders and Emanuel 1977; LeMone 1983; Gao et al. 1990; Gallus and Johnson 1992; Yang and Houze 1996; Trier et al. 1998; Mechem et al. 2006). Such studies all describe the challenges inherent to studying CMT within these systems: unlike many thermodynamic variables, momentum suffers the added complexity imposed by nonconservative effects due to pressure perturbation forces—thus, determining the role of CMT is decidedly more difficult in comparison with convective tendencies of other conserved quantities. In addition to the effect of CMT on large-scale and tropical circulations, some papers investigating derechoes and related MCS phenomena also highlight the potential importance of momentum transport as a key determinant of surface wind speed (a small number of studies also indirectly mention relevance to MCS motion; e.g., Brandes 1977; Johns and Hirt 1987; Johns and Doswell 1992; Vescio and Johnson 1992; Weisman 1992, 1993; Corfidi et al. 1996; Geerts 2001; Corfidi 2003; van den Broeke et al. 2005).

b. MCS momentum transport

Although CMT is not typically listed among the major processes by which MCSs translate through their surrounding environments (e.g., Fritsch and Forbes 2001; Houze 2004), the process in general has been examined in both observational and modeling studies. The two main branches of flow in and around an MCS that can be associated with strong vertical momentum transport are shown in Fig. 1. The momentum field of the MCS can be described by the anelastic equation of motion:

$$\frac{\partial \mathbf{U}}{\partial t} = -\frac{1}{\rho_0}\nabla p' + B\hat{k} - \mathbf{U}\cdot\nabla\mathbf{U} - 2\Omega \times \mathbf{U}, \qquad (1)$$

where $\mathbf{U}$ represents the three-dimensional wind field, p' is the pressure perturbation from the hydrostatic base state, $B = -g(\rho'/\rho_0 - q_h)$, q_h is the hydrometeor mixing ratio, friction is ignored, and the rest of the terms retain their usual meanings.

The generation and evolution of the RIJ is largely described by the perturbation pressure gradient and buoyancy forces in (1). The RIJ is accelerated by the perturbation pressure gradient force that results from the midlevel mesolow (itself a result of the vertical profile of latent heating), and the descent of the accelerated RIJ is largely attributable to negative buoyancy in the trailing stratiform region that arises because of melting, sublimation, evaporation, and water loading (e.g., Srivastava 1987; Braun and Houze 1997; Grim et al. 2009). It has been shown that in some cases, the RIJ helps to maintain the surface cold pool, again via thermodynamic enhancement of environmental cooling (i.e., increasing negative buoyancy by introducing dry environmental air into which falling hydrometeors may melt, evaporate, or sublimate), as well as by increasing cold pool wind speeds through dynamical processes such as downward momentum transport [accounted for in the advection term in (1)] (e.g., Smull and Houze 1987; Haertel and Johnson 2000; Houze et al. 2000; Mechem et al. 2006). Here, we hypothesize that CMT may impact MCS motion in two possible ways:

1) The advective component of MCS motion may be enhanced via the forward penetration of elevated

portions of the RIJ. This scenario describes high-momentum air from aloft being transported forward (and to a lesser extent downward, but not into the surface-based cold pool).

2) System speed may increase as downward CMT increases the speed of the cold pool itself (by increasing the speed of the winds within it); the MCS thus moves more quickly as new convection forms on the faster-moving cold pool boundary.

We will address these possibilities in section 4.

3. Methodology

a. Quasi-idealized modeling approach

To examine an MCS that is simplified for clarity of analysis but that also develops in a three-dimensional, thermal wind–balanced environment, the Weather Research and Forecasting (WRF; Skamarock et al. 2007) model is used in a way that employs a combination of real-case and idealized modeling techniques. This combination benefits from the lucidity of idealized simulations by using simplified initial and boundary conditions that remove small-scale features and perturbations found in observations, while also taking advantage of a real-case modeling framework able to employ a more complete suite of physics options. The simulation also includes a background baroclinic environment (an element largely neglected by many purely idealized modeling studies of the past). This approach allows a more realistic treatment of the larger-scale environment by including an upper-level jet stream that is in thermal wind balance, and accounting for the influence of the Coriolis force on MCS evolution (important to MCS motion over extended time intervals); Skamarock et al. (1994), Jewett and Wilhelmson (2006), and Richardson et al. (2007) also discuss the advantages of such a framework.

A more traditional approach, in which horizontally homogeneous initial conditions were employed and the Coriolis force was neglected, was also tested in order to explore the ramifications of this alternative to more idealized MCS modeling. Comparison of the two methods reveals findings that closely mirror those of past comparison studies such as Skamarock et al. (1994). That is, both approaches result in a quasi-linear MCS that moves in a generally eastward direction and share similar features and system-scale dynamics [e.g., the presence of a midlevel mesolow, subcloud cold pool, and descending RIJ (not shown)]. However, MCS motion is markedly different between the two frameworks; the full-Coriolis simulation moves toward the southeast, likely the combined result of several relevant processes, including Coriolis torque on low-level winds in the cold pool as well as enhanced CAPE toward the south (e.g., Skamarock et al. 1994), in a manner that more closely resembles the motion of observed midlatitude MCS cases that motivate this work. In contrast, simulations using horizontally homogeneous initial conditions and neglecting the Coriolis force produce an MCS that moves due eastward (not shown). Because this study seeks to examine the motion of observed midlatitude MCSs and thereby eventually improve the prediction of MCS motion, the ''quasi idealized'' approach is employed herein.

Initial conditions for the simulation are generated using empirical relationships to produce a simple westerly jet stream in an environment with CAPE and a horizontal wind field in thermal wind balance. Figure 2 shows the initial height and wind fields in the x–y plane as well as in a north–south vertical cross section, in addition to the surface-based CAPE and CIN fields, and Fig. 3 shows the initial sounding. To produce a jet stream and achieve thermal wind balance, the entire initial sounding is first uniformly nudged to be cooler (warmer) as latitude increases (decreases); in this way, the initial conditions more realistically represent the baroclinic background environment common to midlatitude MCSs (relative to more idealized studies in which a single uniform initial sounding is often used). The initial thermodynamic profile is an adaptation of that used in Weisman and Klemp (1982) such that characteristics of MCS environments noted in later studies (e.g., Bluestein and Jain 1985; Houze et al. 1990; Parker and Johnson 2004) are also incorporated. These modifications include drying upper levels by ~10% of their original value, and also adding a weak capping inversion in order to prevent ubiquitous convective initiation in the initially unstable atmosphere. The initial geopotential height and wind fields are produced by first calculating the virtual temperature from the sounding temperature and moisture values. Next, the geopotential height is computed from virtual temperature, and the geostrophic wind field is finally derived from the geopotential height field.

The convection is triggered by a 2°C warm bubble (with unchanged mixing ratio) with horizontal dimensions 4 km × 1 km located between the surface and 3 km. Several experiments were conducted to examine sensitivity to the trigger but little impact was found; cold and warm anomalies of varying sizes, depths, and intensities all ultimately produce very similar MCSs.

The resulting input files are then used by the three-dimensional ''real'' WRF model to generate an MCS that possesses many of the features found in observed cases. An inner domain with 1-km horizontal grid spacing (676 km × 604 km; Fig. 2a) lies within an outer domain of 4-km grid spacing (1800 km × 1800 km). Neither domain utilizes a CP scheme, but both employ

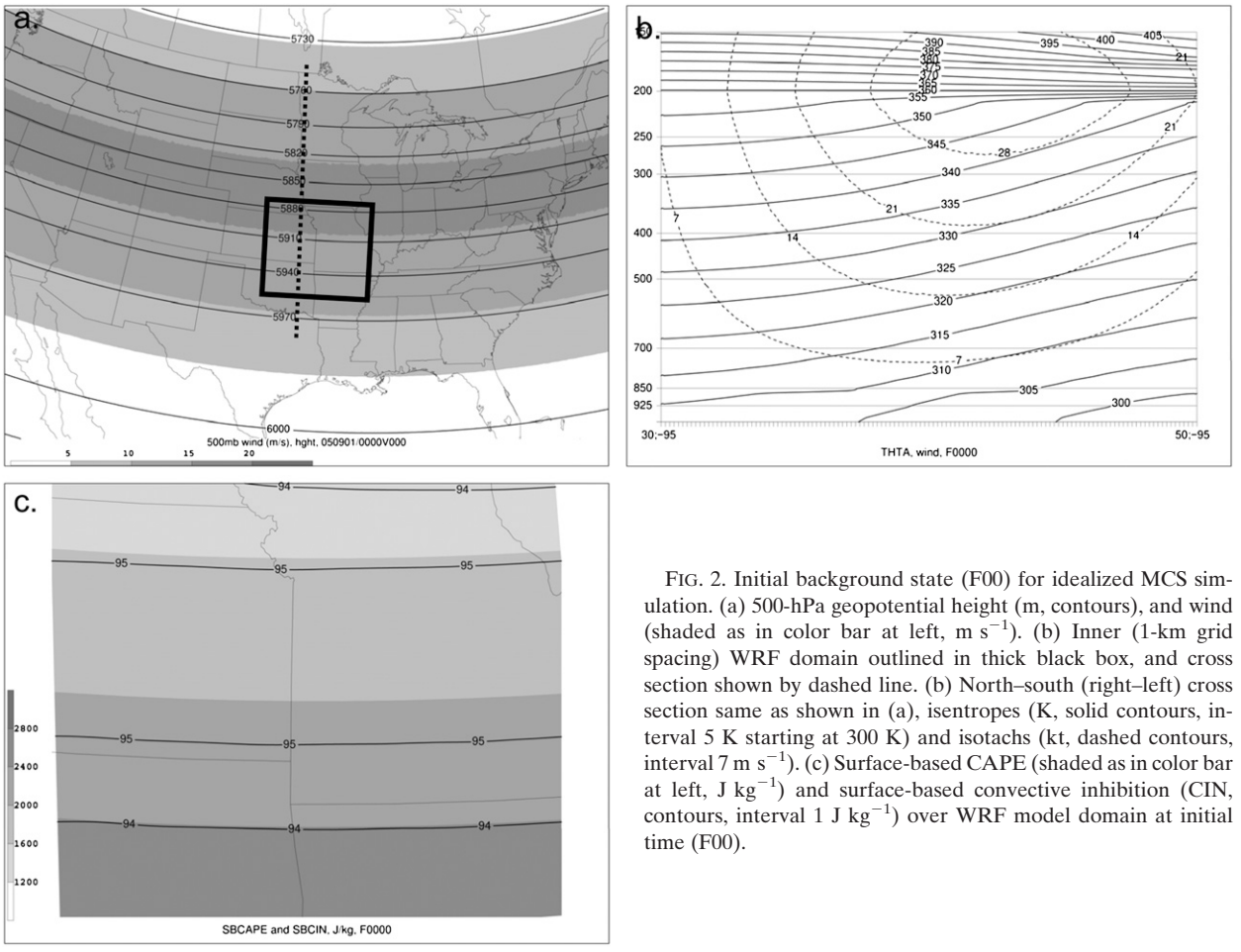

FIG. 2. Initial background state (F00) for idealized MCS simulation. (a) 500-hPa geopotential height (m, contours), and wind (shaded as in color bar at left, m s^{-1}). (b) Inner (1-km grid spacing) WRF domain outlined in thick black box, and cross section shown by dashed line. (b) North–south (right–left) cross section same as shown in (a), isentropes (K, solid contours, interval 5 K starting at 300 K) and isotachs (kt, dashed contours, interval 7 m s^{-1}). (c) Surface-based CAPE (shaded as in color bar at left, J kg^{-1}) and surface-based convective inhibition (CIN, contours, interval 1 J kg^{-1}) over WRF model domain at initial time (F00).

the Yonsei University (YSU) planetary boundary layer (PBL) scheme (Hong et al. 2006) to more completely represent the effects of surface friction and above-ground turbulence that are otherwise not resolved by 1-km grid spacing but are important to accurately represent MCS motion. Model simulation times are hereafter denoted by ''forecast time'' FHH or FHH:mm, specifying the number of hours (HH) and minutes (mm) into the simulation. Further details of the WRF model setup for the simulation are presented in Table 1.

b. Momentum budget methodology

To isolate the effect of CMT on MCS motion, an Eulerian storm-relative momentum budget is computed for the MCS simulation based on the general methodologies of Trier et al. (1998) and Mechem et al. (2006). The momentum budget is also evaluated in order to (i) determine which terms in the momentum equation contribute most to the enhanced wind speeds in the leading portion of the cold pool, and (ii) to obtain a momentum budget of an MCS against which to ultimately compare CMT in MCSs of varying background environments, or in simulations that utilize a CP scheme. To accomplish this, WRF model output is used to compute the terms of the horizontal momentum equation[2]:

$$\frac{\partial \mathbf{V}}{\partial t} = -\mathbf{U} \cdot \nabla \mathbf{V} - f\hat{k} \times \mathbf{V} - \frac{1}{\rho}\nabla p + R, \qquad (2)$$

where $\mathbf{V}$ is the horizontal wind and R denotes a residual, detailed below. To focus on the acceleration of the system and the associated roles of the various budget terms, $\mathbf{V}$ (with x and y components u and v) is defined as the sum of MCS motion and storm-relative wind speeds; that is, $u = u_{SR} + c_x$ and $v = v_{SR} + c_y$, where c_x and c_y are the speeds at which the MCS moves in the east–west and

[2] From (2), it is apparent that rather than assessing the full momentum fields, this framework actually examines the velocity tendency (i.e., acceleration) per unit mass.

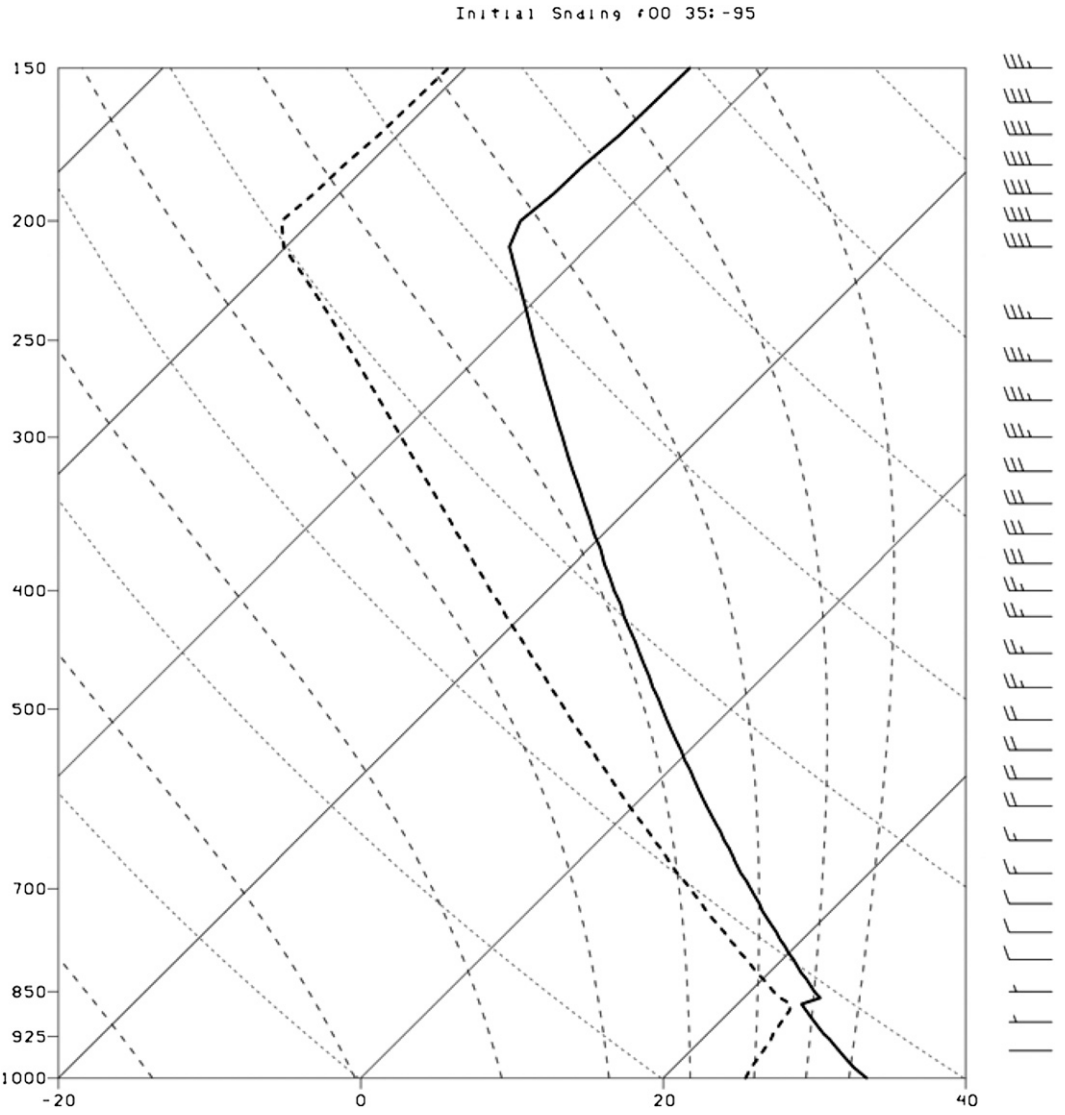

FIG. 3. Initial sounding shape used to initialize the quasi-idealized MCS simulation (at 35°N, 95°W). Temperature (°C, solid line), dewpoint (°C, dashed line), wind barbs (kt) at right.

north–south directions, respectively. After substituting these values and differentiating the basic state and perturbation variables using overbars and primes, the scalar components of (2) become

$$\underbrace{\frac{\partial u}{\partial t}+c_x\frac{\partial u}{\partial x}+c_y\frac{\partial u}{\partial y}}_{\mathrm{TEN}_x}=\underbrace{-(u-c_x)\frac{\partial u}{\partial x}}_{\mathrm{HA}u_x}\underbrace{-(v-c_y)\frac{\partial u}{\partial y}}_{\mathrm{HA}u_y}\underbrace{-w\frac{\partial u'}{\partial z}}_{\mathrm{VA}u'}\underbrace{-w\frac{\partial \overline{u}}{\partial z}}_{\mathrm{VA}\overline{u}}\underbrace{+fv}_{\mathrm{COR}_x}\underbrace{-\frac{1}{\rho}\frac{\partial p}{\partial x}}_{\mathrm{PGA}_x}\underbrace{+R}_{\mathrm{RES}_x}\quad\text{and}\tag{3}$$

$$\underbrace{\frac{\partial v}{\partial t}+c_x\frac{\partial v}{\partial x}+c_y\frac{\partial v}{\partial y}}_{\mathrm{TEN}_y}=\underbrace{-(u-c_x)\frac{\partial v}{\partial x}}_{\mathrm{HA}v_x}\underbrace{-(v-c_y)\frac{\partial v}{\partial y}}_{\mathrm{HA}v_y}\underbrace{-w\frac{\partial v'}{\partial z}}_{\mathrm{VA}v'}\underbrace{-fu}_{\mathrm{COR}_y}\underbrace{-\frac{1}{\rho}\frac{\partial p}{\partial y}}_{\mathrm{PGA}_y}\underbrace{+R}_{\mathrm{RES}_y},\tag{4}$$

where $\overline{u}$ is the grid-relative background (initial) wind field (i.e., u at F00), $u' = u - \overline{u}$ (with the same convention applied to v), and the other terms have their usual meanings. MCS translational speed (c_x, c_y) is calculated

TABLE 1. WRF model setup and parameterization.

Model version	WRF (ARW), version 2.2
Duration	0000 UTC initialization; run out 12 h; output every 5 min
Grid	1-km grid spacing (within a 4-km outer nest)
	676 × 604 gridpoint domain (outer domain 450 × 450)
	31 vertical levels
Physics	Explicit convection (no CP scheme)
	Purdue Lin microphysics
	YSU PBL scheme*
	No radiation or land surface schemes employed; surface fluxes off
Initial conditions	Initial conditions projected on World Meteorological Organization (WMO) 218 grid, with 12-km grid spacing (terrain removed)

* Model sensitivity experiments showed that the organization and movement of the MCS displayed limited sensitivity to the PBL and turbulence/diffusion parameterizations chosen.

by averaging the distance covered per 1-h period by the leading edge of the convection (as denoted by simulated composite radar reflectivity >40 dBZ); making the momentum budget storm-relative avoids the dominance of the horizontal advection terms and highlights those processes that contribute to changes in MCS motion rather than maintenance of constant MCS speed. Also, note that the vertical advection of the background u wind field $\overline{u}$ (VA$\overline{u}$) is distinguished from the vertical advection of the perturbation wind field (VAu', VAv') so that the specific role of each process may be assessed and compared. The residual term, RES, accounts for the combination of ''subgrid-scale effects,'' as termed by Mechem et al. (2006); this term is small, and never exceeds 10% of the total budget. RES includes the errors inherent in calculating the left-hand-side local tendency terms in (3) and (4), as well as our neglect of numerical diffusion and PBL and turbulent flux tendencies. Thus, it largely represents the retarding force of friction close to the earth's surface and mixing in convective updrafts [as reflected by relatively large near-surface and updraft PBL parameterization momentum tendencies (not shown)]. The TEN terms are calculated by taking a centered-difference time derivative for u and v at each output time, with $\Delta t = 5$ min. The terms in (3) and (4) are computed for all of the 5-min output intervals of the simulation, then averaged over 30-min intervals centered about :00 and :30 of every hour; although the system moves throughout each 30-min interval, the temporal averaging reduces noise, allowing assessment of the processes of interest.

Finally, to supplement the Eulerian momentum budget described above, a Lagrangian momentum budget is also performed using parcel trajectories. In doing so, we examine only the forces and accelerations a parcel experiences as it descends from the RIJ-level and into the cold pool, as described by

$$\frac{d\mathbf{V}}{dt} = -\frac{1}{\rho}\nabla p - f\mathbf{k} \times \mathbf{V} + R, \tag{5}$$

where R is analogous to RES in (3) and (4). The Lagrangian perspective more clearly illustrates the integrated accelerations along parcel paths. The transport of momentum can then be understood in terms of the rearrangement of these parcels over time.

4. Results

a. MCS simulation analysis

1) STRUCTURE

The evolution of the simulated MCS is illustrated by the simulated radar reflectivity at 3-h intervals (Fig. 4). The system organizes into a quasi-linear, bowing MCS that exhibits an intense leading convective line followed by a smaller region of lighter precipitation, generally reflecting the classic ''leading convective-trailing stratiform'' MCS structure (e.g., Newton 1950; Houze et al. 1990) [despite the propensity of numerical simulations (particularly those employing bulk microphysics parameterizations) to underrepresent stratiform precipitation (e.g., Lynn et al. 2005; Gallus and Pfeifer 2008; Morrison et al. 2009)]. The cross sections shown in Fig. 5 illustrate the development of the descending RIJ during the system's developing (mature) stage in Fig. 5a (Fig. 5c). The descending RIJ originates around the 4–5-km level in the rear of the system and lowers into the cold pool as the trailing stratiform region develops; this evolution is illustrated by the sloping wind maximum and the ground-relative perturbation wind vectors. The front-to-rear flow branch as depicted by Fig. 1 is implied by an area of weak easterlies aloft, as winds in the storm-relative sense flow from east to west above 5 km

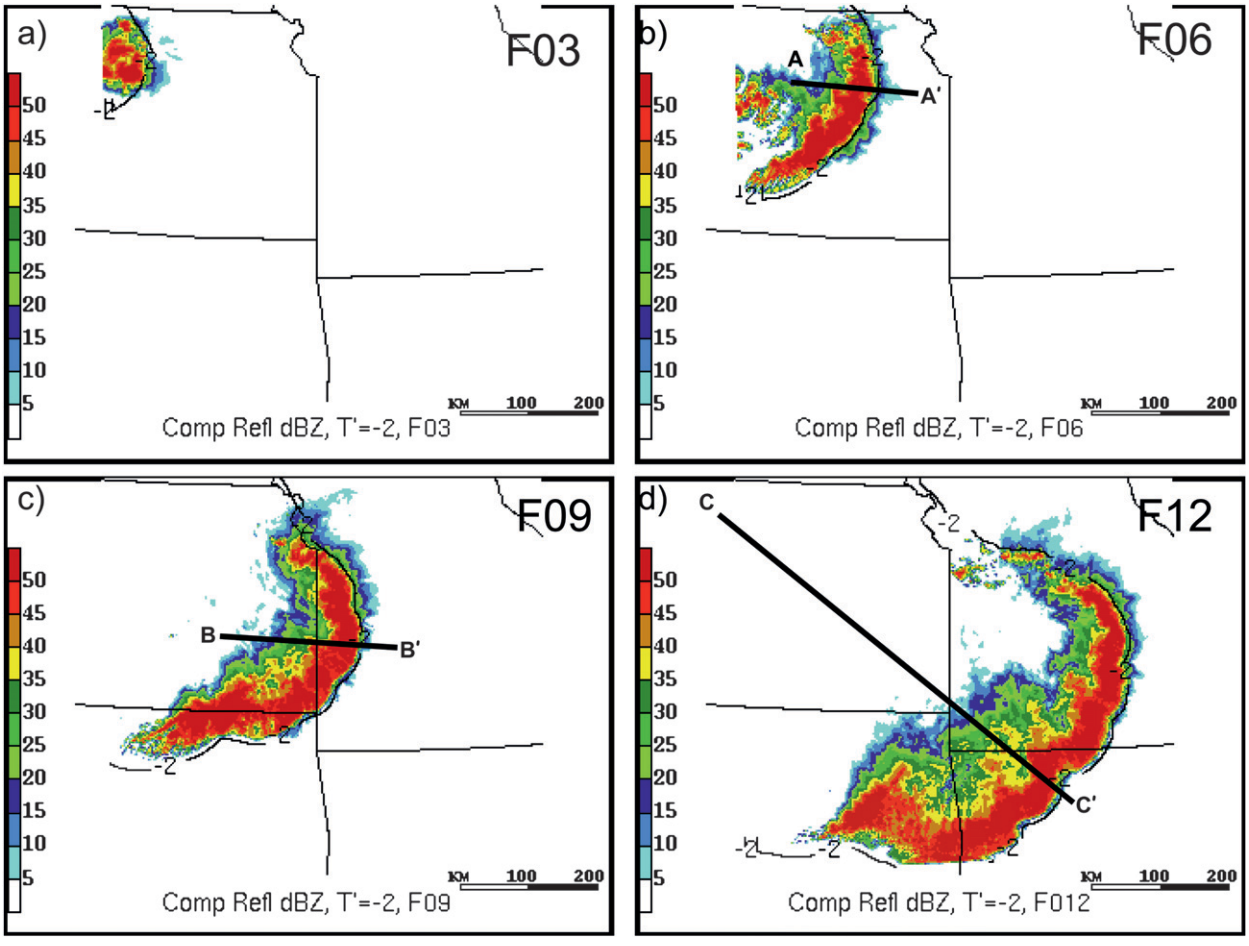

FIG. 4. Simulated composite reflectivity (dBZ, shaded as indicated at right) and cold pool outline [$T' = -2$°C at 0 m (black, solid)], at (a) F03, (b) F06, (c) F09, and (d) F12. Lines A–A′, B–B′, and C–C′ in (b)–(d) depict cross sections shown in subsequent figures; distance (km) as denoted by the scale legend.

(not shown). The perturbation pressure field (Figs. 5b,d) also illustrates dynamical features that compare favorably with past observational and modeling studies of 3D MCSs (e.g., Trier et al. 1998; Houze 2004), such as the deepening of the pressure minimum located just to the rear of the leading convective line and the increased pressure aloft (above 10 km)—a surface-based mesohigh is also present but has a diluted signature in Fig. 5 because of the deep midlevel mesolow just above it. This pattern is consistent with the hydrostatic response to a convective heating maximum overlying a surface cold pool, and the associated acceleration of the rear-to-front and front-to-rear flow matches the findings of studies such as LeMone (1983), Zhang et al. (1989), and Yang and Houze (1996). Therefore, this simulated MCS appears to be a credible representation of the types of systems in which we are interested, and offers the opportunity to use the model output to more closely investigate the CMT process.

2) MCS MOTION

To understand the nature of the simulated MCS motion, the evolution of the MCS and its cold pool from the developing to mature stages is analyzed (Fig. 6). As the system matures and intensifies, the leading edge of the cold pool remains adjacent to the leading line of new convection, implying continuous cold pool forcing for new convection (Fig. 6). Strong low-level convergence is maximized at the leading edge of the cold pool, over which air is forced upward (e.g., Charba 1974; Rotunno et al. 1988). This upward motion and the maximum of low-level convergence are also evident in cross sections across the system's leading edge (e.g., Figs. 5a,c). Thus, the development of new cells along the outflow boundary illustrates that the MCS is ''gust front driven'' in the manner described by Weisman and Klemp (1986).

Using the $T' = -2$°C isosurface to define the three-dimensional cold pool boundary, the average cold pool

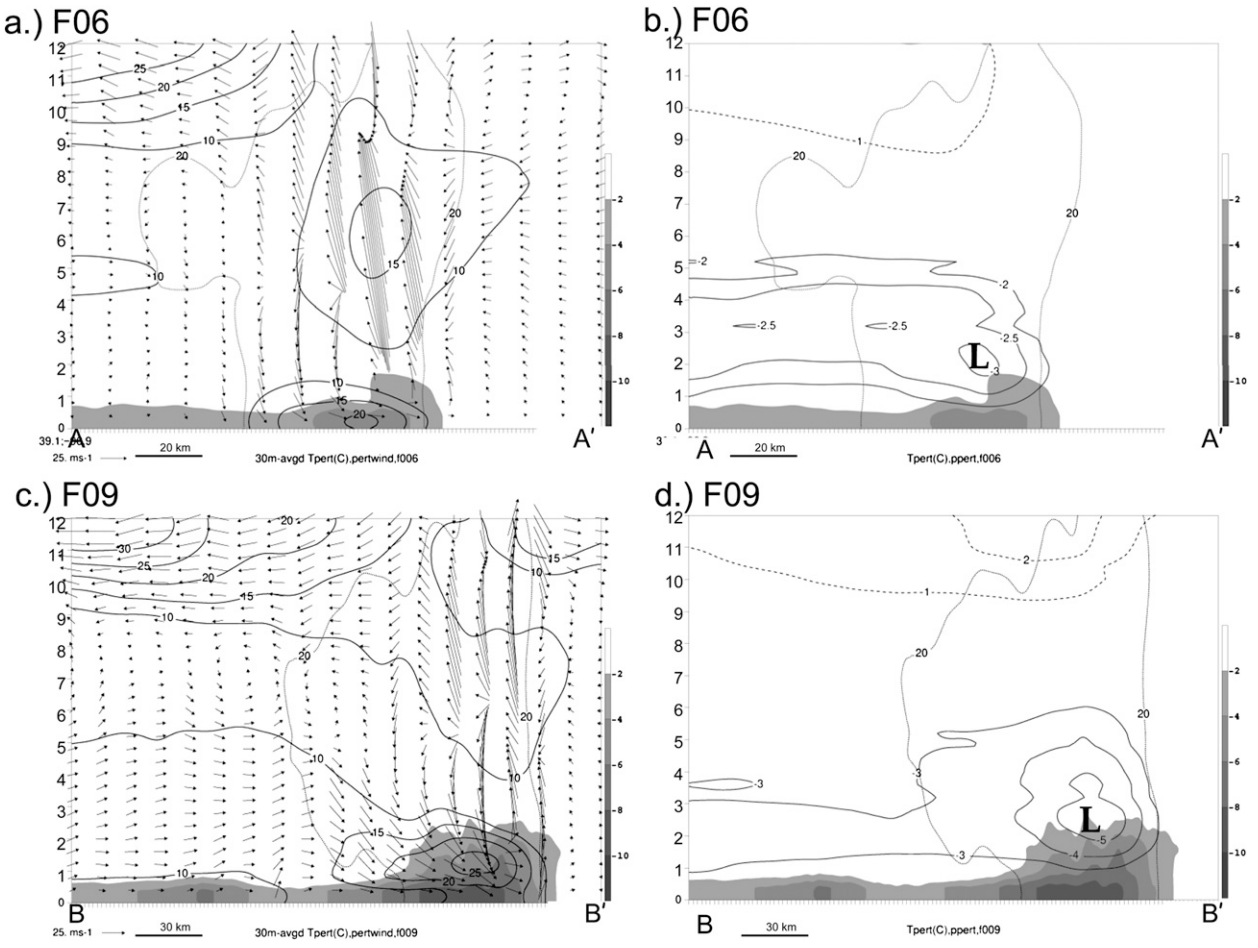

FIG. 5. (a) East–west cross section along line A–A′ as in Fig. 4b at F06. Cold pool (shaded as shown beginning at $T' = -2$°C), magnitude of total perturbation wind $[(u'^2 + v'^2)^{1/2}$, m s$^{-1}]$ and simulated reflectivity (dBZ, gray dotted contour, 20 dBZ). Black arrows show ground-relative perturbation flow in the x–z plane scaled as shown by reference vector in lower-left corner. (b) As in (a), but solid (dashed) contours represent negative (positive) pressure perturbation (hPa). (c) As in (a), but along B–B′ as in Fig. 4c at F09. (d) As in (b), but along B–B′ as in Fig. 4c at F09.

depth is ~1.5 km (ranging from 1 km along the northern and southern ends of the line to nearly 4 km at the MCS apex). The maximum temperature perturbation generally approaches −10°C at the surface and averages −6°C through its depth; such values are consistent with those found by previous observational and modeling studies (e.g., Engerer et al. 2008). The speed at which the cold pool moves can be calculated by its theoretical density current speed c [e.g., Bluestein 1993, his Eq. (2.5.270)]. However, it is known that this expression often does not match the true surface speed of the cold pool and MCS, and that the theoretical speed based on density within the cold pool alone may overestimate the actual cold pool speed by as much as 100% (e.g., Bryan and Rotunno 2008). Despite the strong sensitivity of buoyancy-based cold pool calculations to relatively small thermal and pressure perturbations, we wish to establish an estimate of theoretical cold pool speed here. Thus, we adopt the modified expression suggested by studies such as Nicholls et al. (1988) and Trier et al. (2006), in which the effects of hydrometeor loading and the mid- to upper-level buoyancy anomalies are included:

$$c = \left[-2g \int_0^H \left(\frac{\theta'}{\theta_0} \right)_{\text{coldpool}} + \int_H^{Z_T} \left(\frac{\theta'}{\theta_0} \right)_{\text{warmcloud}} - \int_0^{Z_T} q_h \, dz \right]^{1/2}, \quad (6)$$

where H is the depth of the cold pool (~2 km), Z_T is the height at which the pressure perturbation above the cloud goes to zero (~14 km), and θ' is the potential temperature perturbation as compared to the base-state θ_0, as defined by along-line averaged vertical profiles in

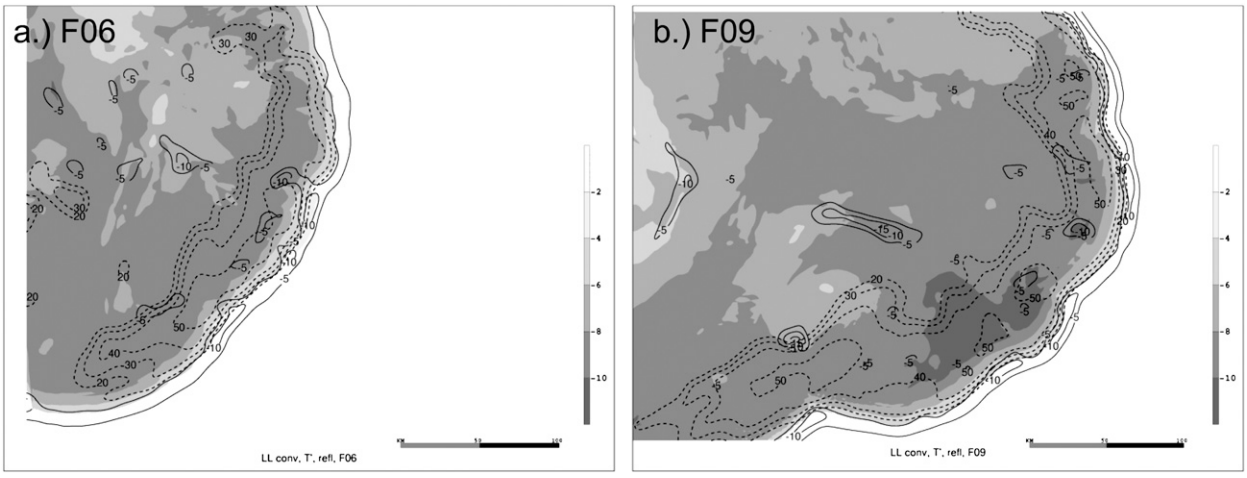

FIG. 6. (a) Low-level (2 m) temperature perturbation from initial environment (K, shaded as in legend at right), divergence (black contours, -5×10^{-4} s^{-1} interval, starting at -5×10^{-4} s^{-1}) at 10 m, and composite reflectivity (dashed, interval 10 dBZ, starting at 20 dBZ) at F06. (b) As in (a), but valid at F09.

the leading 20 km of the cold pool following Trier et al. (2006). Calculations of the theoretical cold pool speed according to (6) are shown in Fig. 7. Differences between the theoretical and observed cold pool speeds, particularly during periods of MCS acceleration (discussed below), indicate that the winds in the cold pool are *not* simply a product of the static pressure field produced by the cold pool.

The advective component of MCS motion is often estimated by measuring the mean wind in the cloud-bearing layer (e.g., Corfidi et al. 1996). Along an approximately east-west moving portion of the MCS, the mean wind speed (u) in the 900–200-hPa layer (e.g., Fritsch and Forbes 2001) from F05 to F12 is ~14 m s^{-1}; the dotted line in Fig. 7 shows the evolution of this field over time.

The translational speed of the system was calculated as detailed in section 3, and the solid line in Fig. 7 shows that the system speed accelerates from about 6 to 22 m s^{-1} from the MCS's initial to mature stages. The dashed line in Fig. 7 illustrates the average value of the maximum wind speed found over the lowest 3 km of each grid column in the leading 40 km of the cold pool (a volume over which additional quantities are averaged in the following section). MCS speed and the average maximum wind speed in the leading portion of the cold pool are relatively closely matched, and the evolution of each field with time is also similar (the two quantities have a correlation coefficient of 0.9 and a root-mean-square error of 2 m s^{-1}); similarly high correspondence is found for the overall average wind speeds in the cold pool even

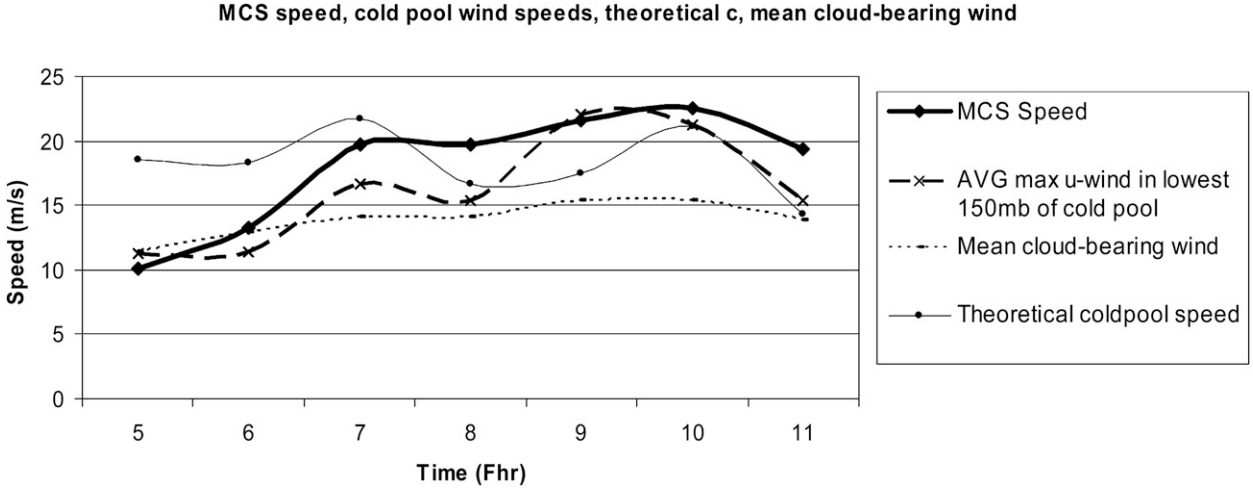

FIG. 7. Speed of MCS (m s^{-1}, solid), average of gridpoint maximum wind speed in the lowest 3 km of the cold pool (m s^{-1}, large dashed), average mean cloud-bearing wind (from 900 to 200 hPa, m s^{-1}, small dashed), and theoretical cold pool speed (m s^{-1}, thin solid).

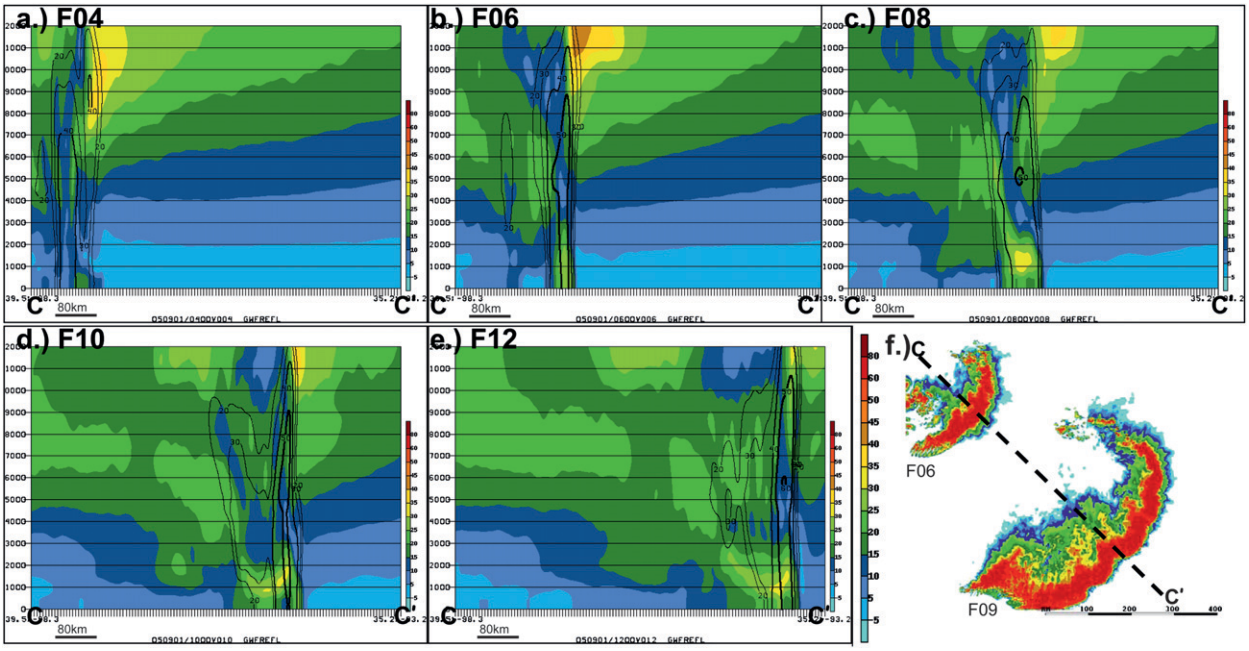

FIG. 8. (a) Total wind speed (m s^{-1}) along line C–C′ shown in Figs. 4d,f (shaded, according to legend at right) and simulated reflectivity (contours, interval 10 dB*Z*, starting at 20 dB*Z*) at F04. (b) As in (a), but for F06. (c) As in (a), but for F08. (d) As in (a), but for F10. (e) As in (a), but for F12. (f) Cross section C–C′ (black, dashed line) and simulated composite reflectivity at times F06 and F09 as labeled and shaded as in Fig. 4.

when slightly different cold pool volume definitions are used. This relationship also implies that the TEN terms in (3) and (4) closely represent the tendency of MCS motion by describing changes in wind speed at the leading edge of the cold pool (Figs. 6 and 7). Thus, the MCS largely moves at the speed of the winds in the leading edge of its cold pool, which is likewise the speed at which the actual cold pool and gust front move (e.g., Goff 1976; Lafore and Moncrieff 1989). Furthermore, comparing the calculated theoretical cold pool speeds to the actual cold pool speeds reveals that the theoretical value not only underestimates (overestimates) the actual value at mature (initial) stages, but also fails to fully explain the period of maximum acceleration from F05 to F07; this suggests that the speed of the cold pool is not driven and/or maintained by density current mechanics alone.

b. CMT in the simulated MCS

1) SYSTEM EVOLUTION AND VERTICAL MOMENTUM FLUXES

The evolution of the wind field along cross-section C–C′ (as in Fig. 4d) illustrates the development and descent of stronger winds (predominantly westerlies) with time, as weaker wind speeds (predominantly weaker westerlies/storm-relative easterlies) ascend in the front-to-rear flow (Fig. 8). Plotting vertical momentum fluxes helps illustrate the CMT process; a downward flux of westerly momentum is evident in the lower rear of the system below 3-km altitude, corresponding to the descending flow of the RIJ (Fig. 9). As the system matures, these flux magnitudes grow considerably toward the leading edge of the cold pool (not shown). Horizontal plots of $-\partial(uw)/\partial z$ (Figs. 9c,e) reveal maximized vertical momentum flux convergence in lower layers (~800 m), consistent with the descending flow of the RIJ and the westerly maximum produced near and below 1.5 km (Figs. 5a,c). This demonstrates the importance of CMT in these lower levels, where the downward transport of momentum maximizes. The behavior of the wind field shown in Fig. 8, as well as the plots of the vertical momentum flux in Fig. 9 depict the descent of the (generally westerly) wind speed maximum from midlevels (4–8 km) in the developing stages of the MCS, to lower levels and approaching the surface as the system matures. Concurring with the findings of Houze et al. (2000) and Mechem et al. (2006), the combination of these sloping, downward motions from areas of stronger winds aloft and the midlevel accelerations provided by the perturbation pressure field (e.g., Fig. 5) indicates that the near-surface wind field of the mature MCS results in part from the downward transport of increased momentum aloft. The contribution from CMT can also explain the discrepancy

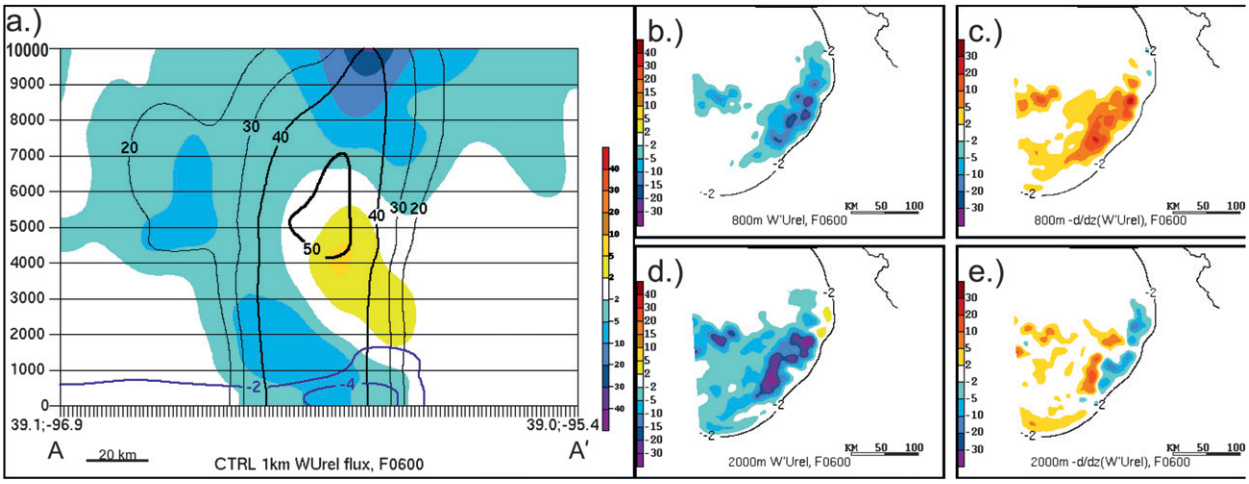

FIG. 9. (a) East–west cross section through leading edge of MCS along line A–A′ at F06 (as shown in Fig. 4b) showing cold pool (T', blue contours, −2°C intervals starting at −4°C), and downward momentum flux (shaded as in legend at right), and simulated radar reflectivity (black contours, 10-dBZ intervals starting at 20 dBZ). (b) Downward momentum flux at 800 m at F09 ($m^2\ s^{-2}$), $T' = -2$°C at 0 m (black, solid). (c) As in (b), but for $-\partial(uw)/\partial z$, where positive values denote convergence ($m\ s^{-2}$). (d) As in (b), but at the 2000-m level. (e) As in (d), but at the 2000-m level.

between the observed cold pool speed of the simulated system and the theoretical cold pool speed calculated above.

2) MOMENTUM BUDGET ANALYSES

As detailed in section 3, two momentum budgets are computed using WRF model output, with the ultimate goals of (i) ascertaining which terms in the momentum equation contribute most to the enhanced wind speeds in the leading portion of the cold pool, and (ii) quantifying the role of CMT in the MCS momentum field and hence its forward motion.

Beginning with the Eulerian framework, a summary of each momentum budget term at 800 m is shown in Fig. 10; this level represents the mid to lower portion of the surface-based cold pool. The **V**-tendency term (TEN) in Fig. 10a represents the sum of left-hand sides of (3) and (4) at F06, which is chosen as the main momentum budget analysis time as it marks the beginning of the period of maximum system acceleration (e.g., Fig. 7). The vectors show general storm-relative forward acceleration along the leading edge of the system, toward the east and southeast. Rearward-pointing vectors located toward the back of the system reflect the deceleration of the wind speeds behind the pressure maximum at the leading edge of the cold pool. At this level and time, the vertical advection term (Fig. 10b) largely determines the acceleration in the forward portion of the cold pool, as evidenced by the southeastward-directed vectors along the front of the MCS. The remaining terms (HA, COR, PGA, and RES terms in Figs. 10c–f, respectively) instead contribute rearward (or small forward) accelerations in these lower levels; thus, they do not appear to be major contributors to the acceleration of the leading line of the MCS (at lower levels). Examination of the budget terms at higher altitudes (not shown) reveals an increase in the PGA and vertical advection terms, particularly in the stratiform region of the system; this pattern is illustrated by the cross sections shown in Fig. 11.

Comparison of the leading budget terms (TEN_x, PGA_x, HAu_x, $VA\overline{u}$, and VAu') at the beginning of the period of maximum MCS acceleration (F06) illustrates the contribution of each term to the low-level westerly wind maximum (Fig. 11). It is clear that in the RIJ region (as depicted by the shaded isotachs) both PGA_x and $VA\overline{u}$ (Figs. 11b,e) are large contributors to MCS zonal acceleration, with PGA_x accelerating the rear inflow, and $VA\overline{u}$ transporting a portion of the background westerlies downward. In the leading convective portion of the MCS, the VAu' term largely determines the positive u-momentum tendency (Fig. 11d), with a contribution in the leading edge of the cold pool from HA (Fig. 11c). While cross sections represent a limited horizontal area, the pattern seen in the four momentum budget terms shown is generally representative of the mean pattern along the line.

To compare and summarize the relative importance of each term in (3), the budget terms are averaged in two system-relative volumes (illustrated in both Fig. 12 and by the outlined boxes in Fig. 13); one at the leading edge of the cold pool ($VOL_{leading}$, Fig. 12a) and the other toward the middle-to-rear portion of the system ($VOL_{trailing}$,

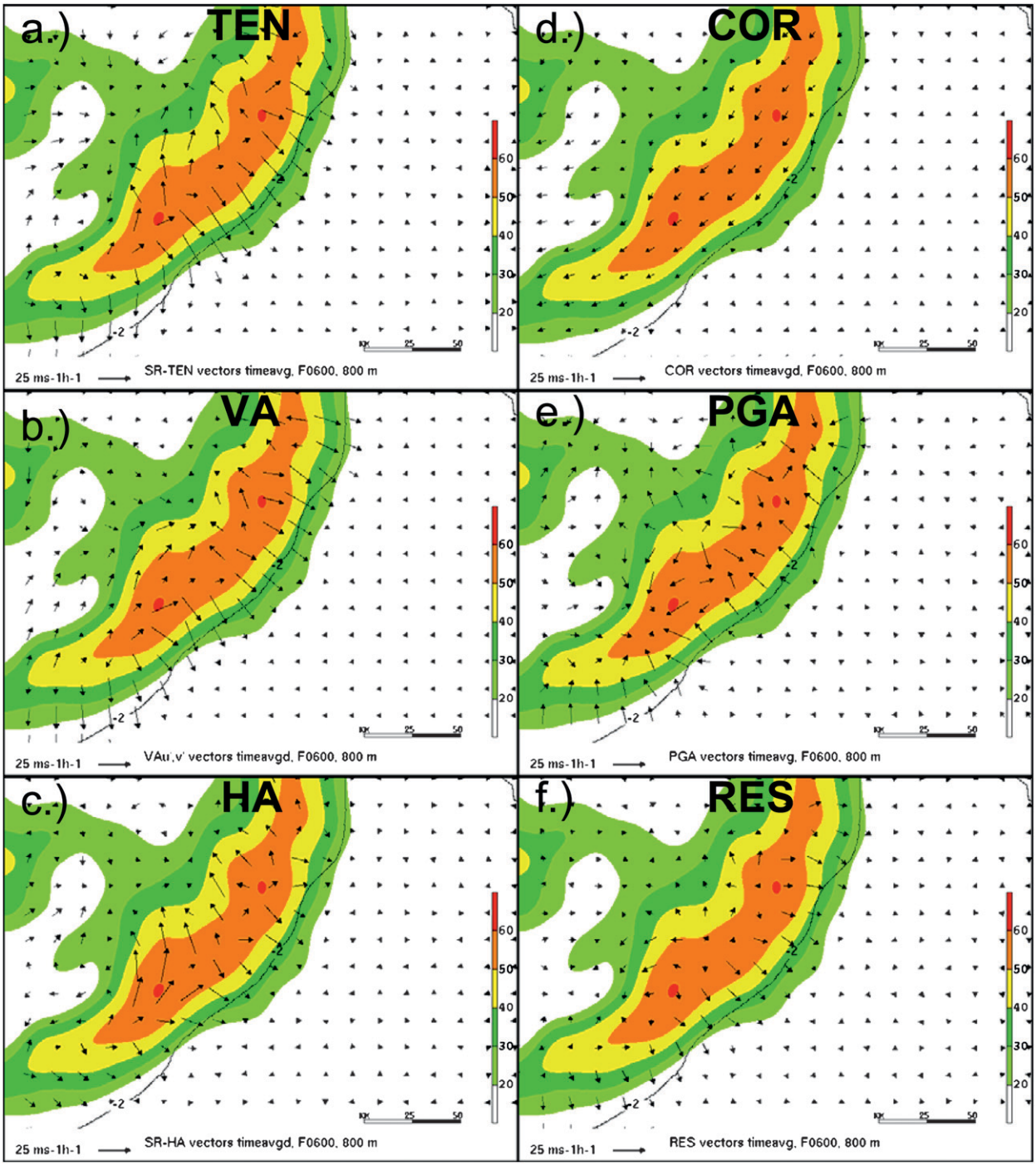

FIG. 10. (a) Simulated reflectivity (dBZ, shaded, as in legend at right), $T' = -2$°C at 0 m (black, solid), and the vector sum of the u- and v-tendency (TEN) terms from Eqs. (3) and (4) (vectors, m s^{-1} h^{-1}, scaled as shown by reference vector in lower-left corner) at 800 m at F06. (b) As in (a), but vectors show VA (i.e., CMT). (c) As in (a), but vectors show HA term. (d) As in (a), but vectors show COR term. (e) As in (a), but vectors show PGF term. (f) As in (a), but vectors show RES term.

Fig. 12b). The volumes are laterally bounded to the north and south according the portion of the system that moves most nearly zonally, and the east–west extent is limited to 0–40 km (40–120 km) behind the leading edge of the cold pool for $\mathrm{VOL}_{\mathrm{leading}}$($\mathrm{VOL}_{\mathrm{trailing}}$). In the storm-following volumes, budget terms are evaluated in the east–west direction only. While 3D effects of a curved system such as this one are likely important near

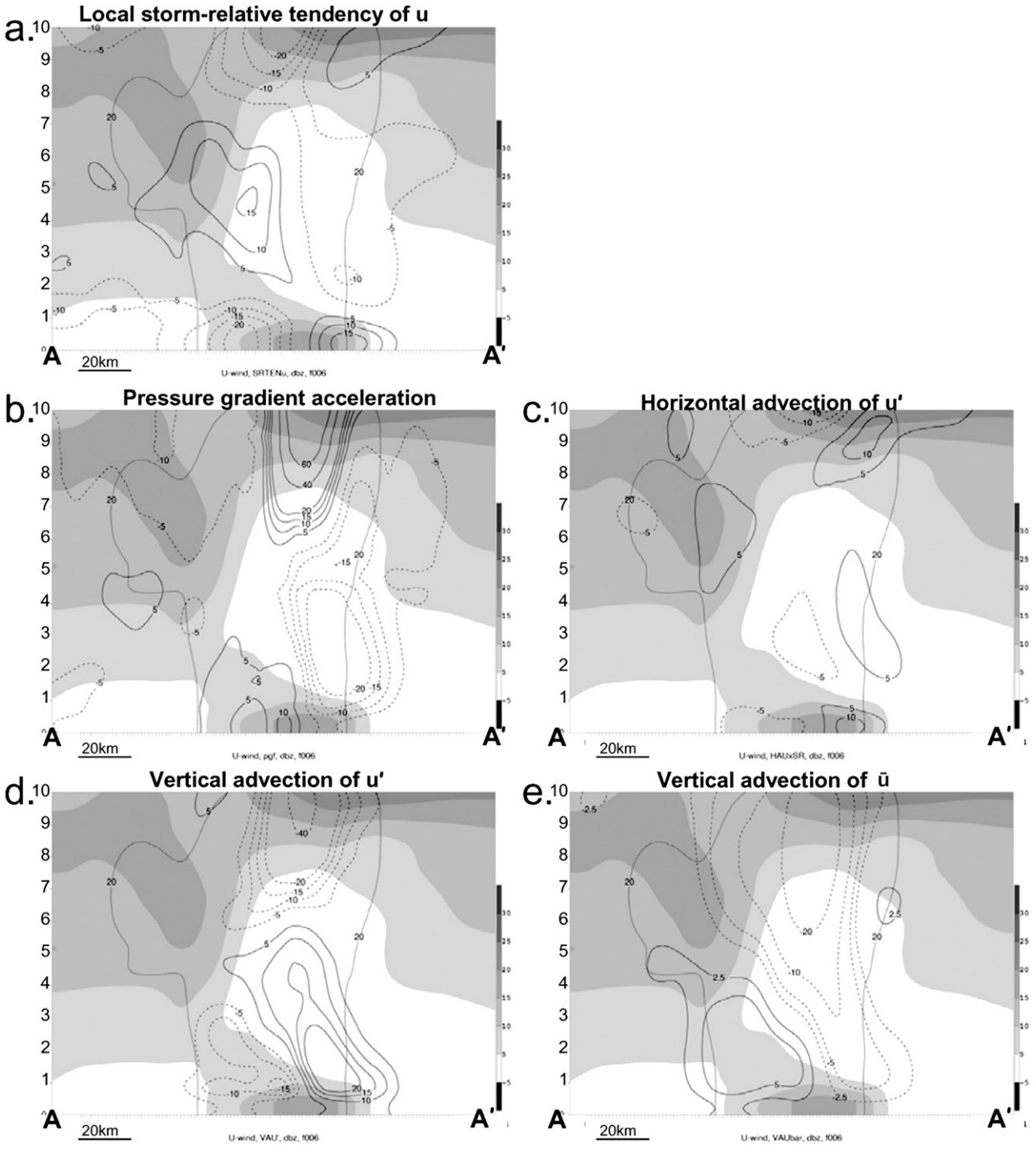

FIG. 11. Cross sections of momentum budget terms along line A–A′ (shown in Fig. 4b) at F06: (a) u (m s^{-1}, shaded as in legend at right) and TEN$_x$ [m s^{-1} h^{-1}, positive (negative) values in solid (dashed) contours], and 30-dBZ contour (dotted) of simulated reflectivity. (b) As in (a), but for PGA$_x$. (c) As in (b), but for HAu_x. (d) As in (a), but for VAu'. (e) As in (a), but for VA$\bar{u}$.

the ends of the line (e.g., Trier et al. 1998), a centrally located and eastward-moving portion of the line is selected such that the x components of motion sufficiently represent the processes of interest. However, in a storm-relative sense (i.e., whether a process acts with or against the system's forward motion) along other portions of the line, the y-component contributions from (4) (and depicted in Fig. 10) are consistent with those examined here. The division of the system into these two volumes mimics many previous MCS momentum budgets, which

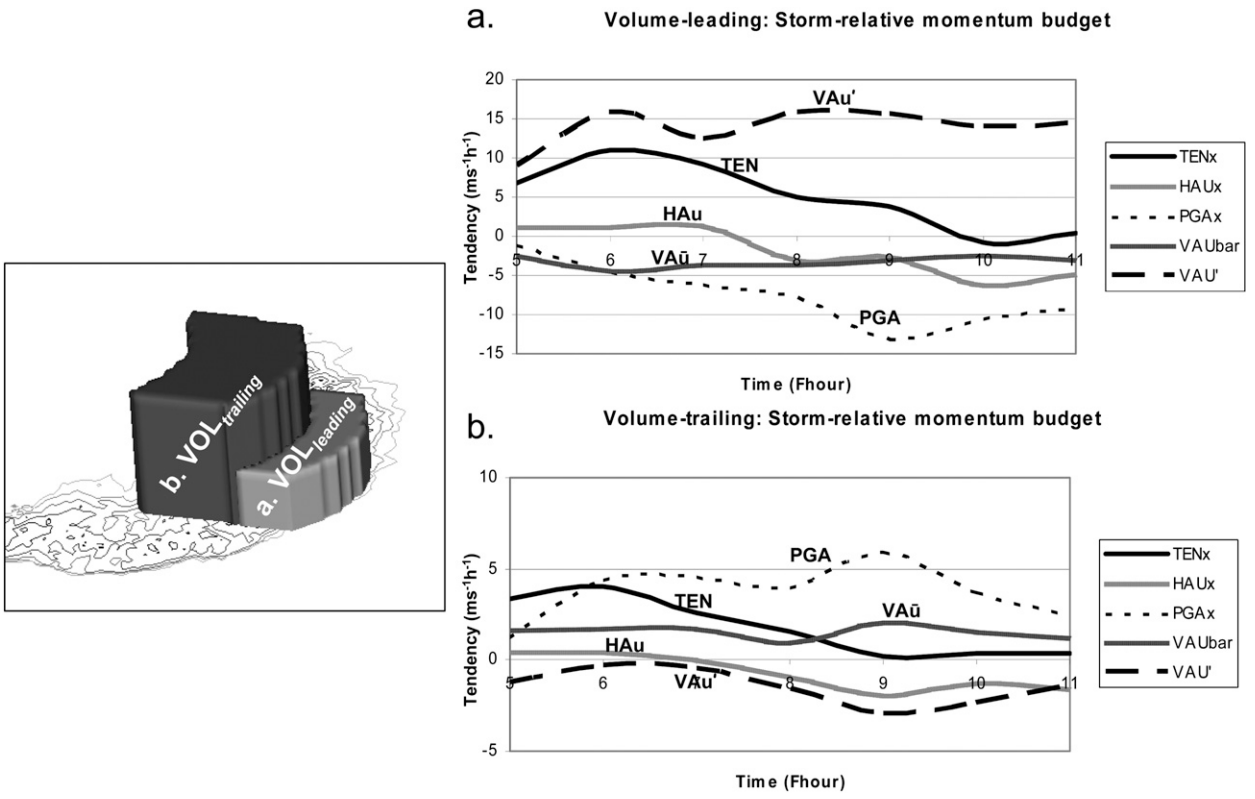

FIG. 12. Volume-averaged momentum budget terms as labeled in key for times F05–F11 for the (a) leading volume and (b) trailing volume (note different scales of y axes).

have divided the system into ''leading (convective)'' and ''trailing (stratiform)'' sections (e.g., Gallus and Johnson 1992; Yang and Houze 1996; Trier et al. 1998; Mechem et al. 2006). Defining the volumes to include lower- to midlevels following the leading edge of the system (0–3 and 0–6 km for $VOL_{leading}$ and $VOL_{trailing}$, respectively) serves to focus on the low-level storm outflow contained within the cold pool and also on the rear-to-front flow branch, which contributes to changes in low-level westerly momentum[3] (e.g., Fig. 1).

Figure 12a reveals a consistent positive contribution from VAu' in $VOL_{leading}$, confirming that the vertical advection of perturbation rear-to-front flow is of first-order importance in strengthening westerly flow in the forward part of the storm. Farther back from the leading line in $VOL_{trailing}$ (Fig. 12b), the vertical advection of the background wind ($VA\bar{u}$) and PGA_x contribute to the local acceleration of the RIJ, while the HAu_x term decreases in time as the strongest westerlies progress toward the leading edge of the cold pool and the system accelerates.

The simulated MCS moves at a speed that very closely matches the average wind speed in the forward portion of the cold pool (i.e., $VOL_{leading}$), as shown in Fig. 7. Therefore, at the leading edge of the MCS, the Eulerian tendency term (TEN) represents the storm-relative acceleration of the momentum field and thus the change in system motion (Fig. 14); strong correlation ($r = 0.97$) between large TEN values and periods of MCS acceleration indicates that the remaining terms in (3) and (4) can provide insight into the contribution of each process to changes in MCS motion. Because of the gust-front-driven nature of system motion, as well as the strong correlation between the winds in the forward portion of the cold pool and the speed at which the MCS moves, we first use the momentum budget volume averages in $VOL_{leading}$ to determine which terms contribute most to the enhanced wind speeds there (Fig. 15). Throughout the lifetime of the system, VAu' adds a large positive contribution to MCS forward motion in the leading volume

[3] Multiple volumes were examined in order to select the most appropriate areas over which to average the terms in (3) and (4); however, little sensitivity was found when increasing or decreasing volume depth or spatial extent within ~1 or 40 km, respectively. The volumes are defined to isolate the rear-to-front flow branch by excluding the front-to-rear flow branch as much as possible, though implications of the front-to-rear flow in the convective region may be addressed in future work.

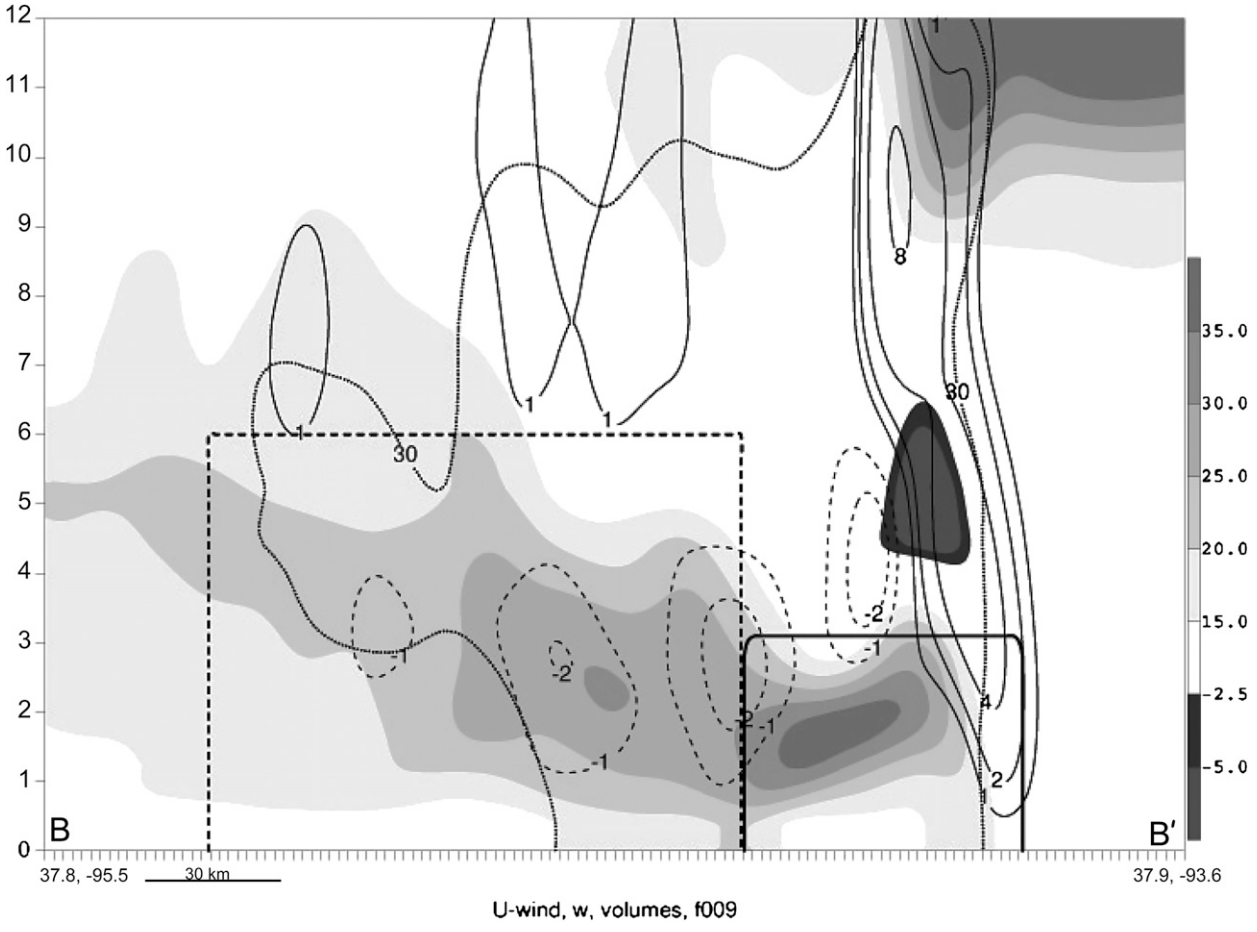

FIG. 13. Cross section of u (shaded, m s^{-1} as in color bar at right), and w [m s^{-1}, positive (negative) black solid (dashed) contours] at F09 along line B-B′ as in Fig. 4c. Solid (dashed) box outlines volumes $\mathrm{VOL}_{\mathrm{leading}}$ ($\mathrm{VOL}_{\mathrm{trailing}}$), and simulated reflectivity contour of 30 dBZ (dotted).

(Fig. 15b). In $\mathrm{VOL}_{\mathrm{leading}}$, $\mathrm{VA}u'$ averages ~13 m s^{-1} h^{-1} throughout the simulation, clearly contributing to the acceleration of the system. The magnitude and evolution of $\mathrm{VA}u'$ relative to the u-momentum tendency at the leading edge of the cold pool (shown by the thick black TEN_x line in Fig. 12) thus illustrate that its contribution to MCS speed is nonnegligible.

As described above, a volume encompassing the mid to rear portion of the storm ($\mathrm{VOL}_{\mathrm{trailing}}$) is also defined in order to diagnose the role of the budget terms in the generally westerly momentum field produced in the RIJ region. Similar to $\mathrm{VOL}_{\mathrm{leading}}$, the tendency values for $\mathrm{VOL}_{\mathrm{trailing}}$ (Fig. 12b) also correlate reasonably well with MCS motion, reinforcing the utility of examining the trailing stratiform region of the storm and its role in the MCS momentum field. Within the trailing volume, it is clear that $\mathrm{VA}u'$ is much smaller than in $\mathrm{VOL}_{\mathrm{leading}}$ (Figs. 15c,f); this is partially due to the volume generally trailing the local u' maximum (Fig. 13), but also reveals a shortcoming of the volume approach. That is, averaging over a jet feature such as u' masks the actual contribution of this field, as its volume average is close to zero. Therefore, while considerable information can be gleaned from the volume-averaged budget for most terms, the role of $\mathrm{VA}u'$ in $\mathrm{VOL}_{\mathrm{trailing}}$ is likely better assessed by alternative approaches such as displays of flux and flux convergence as in Fig. 9. However, the volume-averaging approach does clearly illustrate that in $\mathrm{VOL}_{\mathrm{trailing}}$ there is a relatively modest but significant contribution from both the PGA_x term and the $\mathrm{VA}\overline{u}$ term; both supply a steady acceleration of 2–8 m s^{-1} h^{-1} to the rear-to-front flow in the trailing stratiform portion of the system. From an Eulerian perspective, it is difficult to comment on how these terms contribute specifically to storm motion, given that the overall effect is likely integrated along the sloping RIJ descent (and also that the contribution of both PGA_x and $\mathrm{VA}\overline{u}$ may extend above 6 km in some areas).

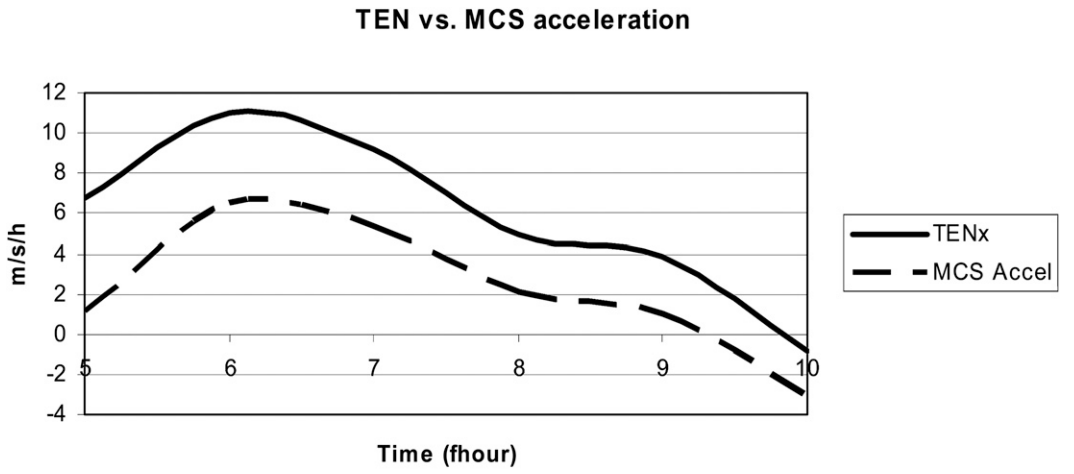

FIG. 14. TEN_x in $VOL_{leading}$ (solid, m s^{-1} h^{-1}) and x component of MCS acceleration (dashed, m s^{-1} h^{-1}) vs time (x axis, h).

By eliminating the advection terms and instead moving *with* the descending parcels, the Lagrangian budget is calculated to more fully understand (i) the local acceleration of the RIJ, (ii) the extent to which PGA impacts MCS motion, and (iii) the connection between the leading and trailing volumes used above, creating a seamless picture of airstream accelerations. The Lagrangian budget computes parcel acceleration and the PGA and COR fields along parcel trajectories, according to (5). Figure 16a shows a composite of 50 trajectories that originate in the RIJ (~5-km altitude at F06), revealing that the average parcel motion sampled is one of descent from midlevels into the cold pool (to within approximately 100 m of the surface) by F11. Along this trajectory, there is a marked period of maximized acceleration, from F07:00 (25 200 s) to F08:25 (30 300 s), during which a strong pressure gradient acceleration exists in the direction of parcel motion (by accounting for the acceleration terms in the

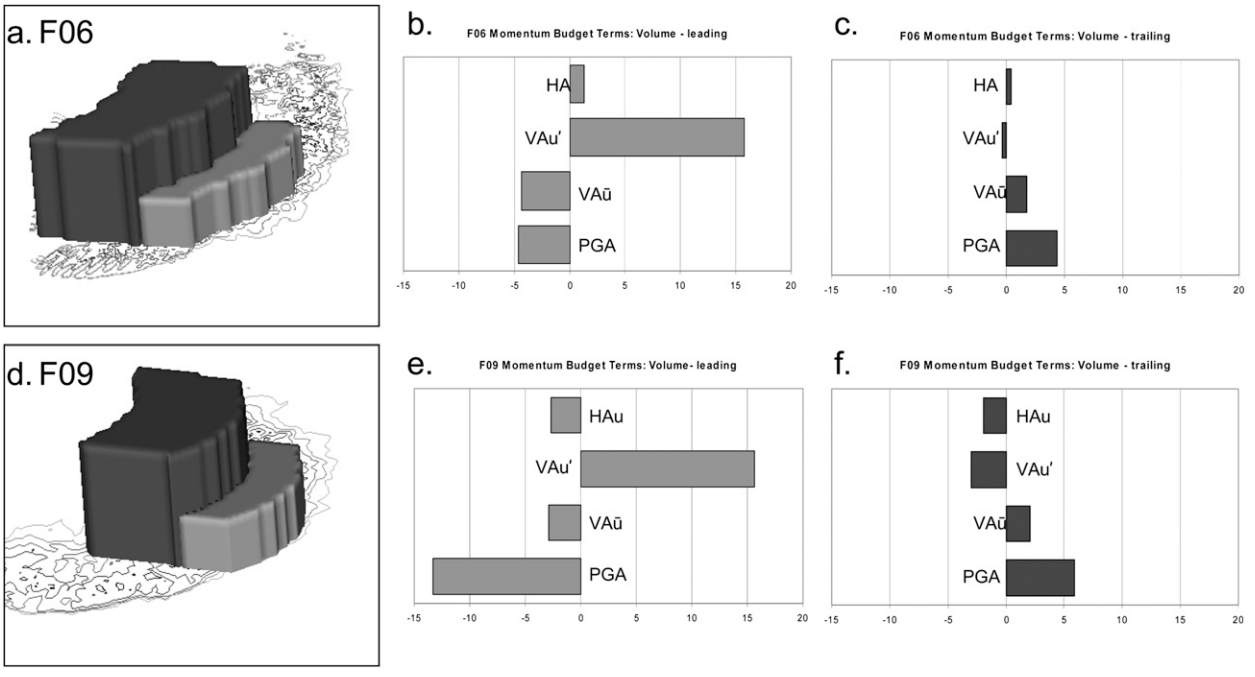

FIG. 15. (a) $VOL_{leading}$ (light gray) and $VOL_{trailing}$ (dark gray) at F06 and (b) momentum budget term averages as labeled over $VOL_{leading}$ at F06 (m s^{-1} h^{-1}). (c) As in (b), but for $VOL_{trailing}$. (d) As in (a), but for F09. (e) As in (b), but for F09. (f) As in (c), but for F09.

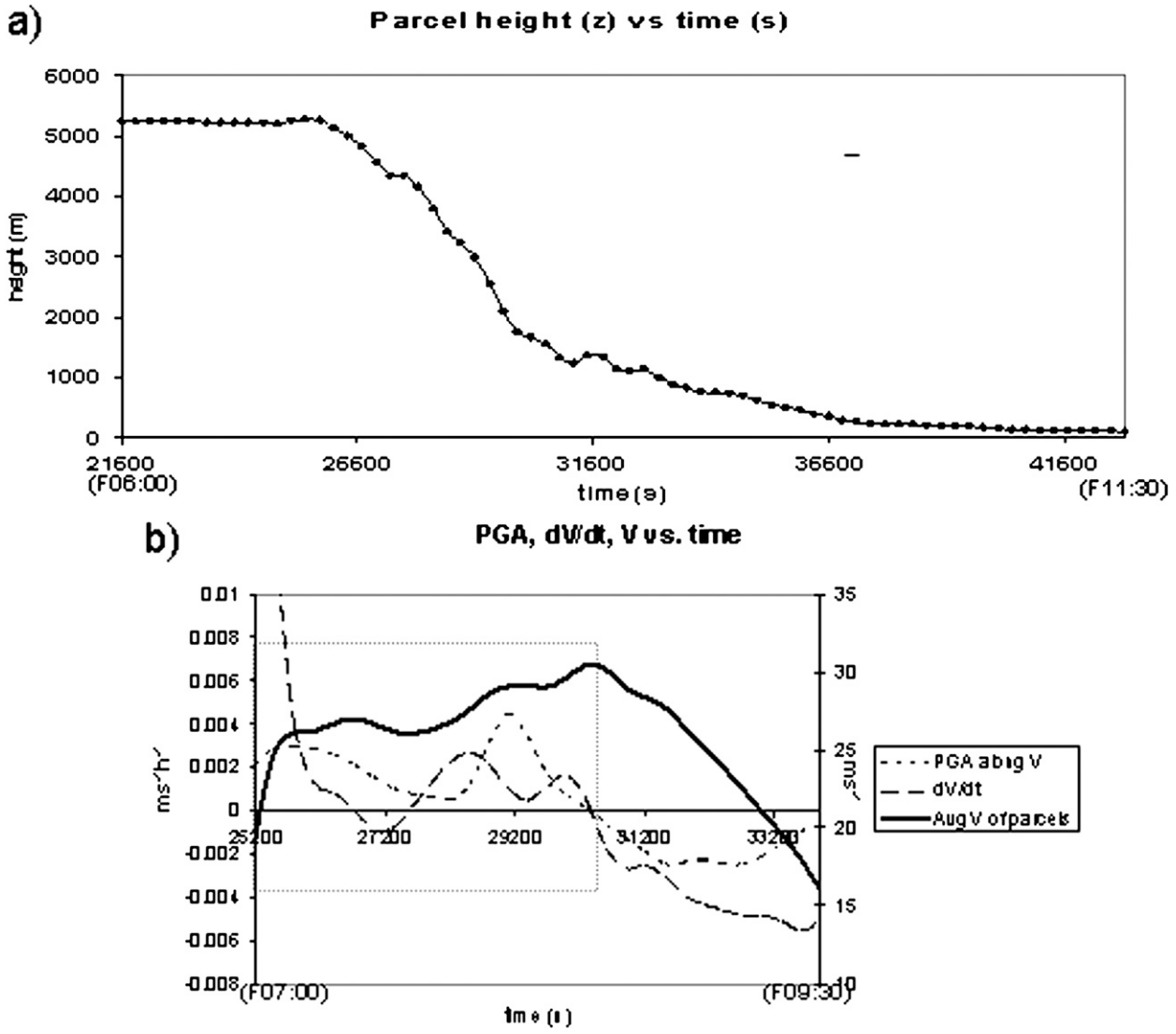

FIG. 16. (a) Height (y axis, m) vs time (x axis, s) of average trajectory of 50 parcels originating at RIJ level at F06. (b) PGA (short dashed, m s^{-2}, values on left y axis), acceleration ($d|V|/dt$, long dashed, m s^{-2}, values on left y axis), and wind speed ($|V|$, solid, m s^{-1}, values on y axis at right) for time period $t = 25\ 200$ s (F07:00) to $t = 34\ 200$ s (F09:30) only. Dotted box in (b) denotes period of acceleration from $t = 25\ 200$ s to $t = 30\ 300$ s.

direction of parcel motion, the Coriolis term may be neglected, as it only acts perpendicular to parcel motion). Over this 85-min time interval, the pressure gradient acceleration accounts for an acceleration of ~8.5 m s^{-1} (its average value ~6 m s^{-1} h^{-1}), and the composite trajectory's average wind speed indeed strengthens by ~9.5 m s^{-1} (Fig. 16b). Because the *PGA* term is the only means by which the MCS momentum field may accelerate or decelerate along a parcel trajectory, we can more clearly define the role of the midlevel mesolow and resulting pressure gradient acceleration in the CMT process.

The Lagrangian budget further illuminates the critical role of downward CMT in bringing the accelerated RIJ flow surfaceward. The parcels experience more than half of their acceleration (nearly 7 m s^{-1}) prior to the steep descent toward the surface [beginning around F07:45 (27 900 s); Fig. 16a], illustrating that vertical advection (i.e., CMT) is a critical process by which cold pool wind speeds and thus MCS speed increase; this is corroborated by the dominance of VAu' in Fig. 12. The combination of the storm-relative Eulerian and Lagrangian budgets illustrate the evolving roles of various forcing terms. Specifically, we see that the PGA term plays an important role in accelerating the RIJ that is then transported downward via vertical advection; similar to the findings of Zhang et al. (2003). The average trajectory path also

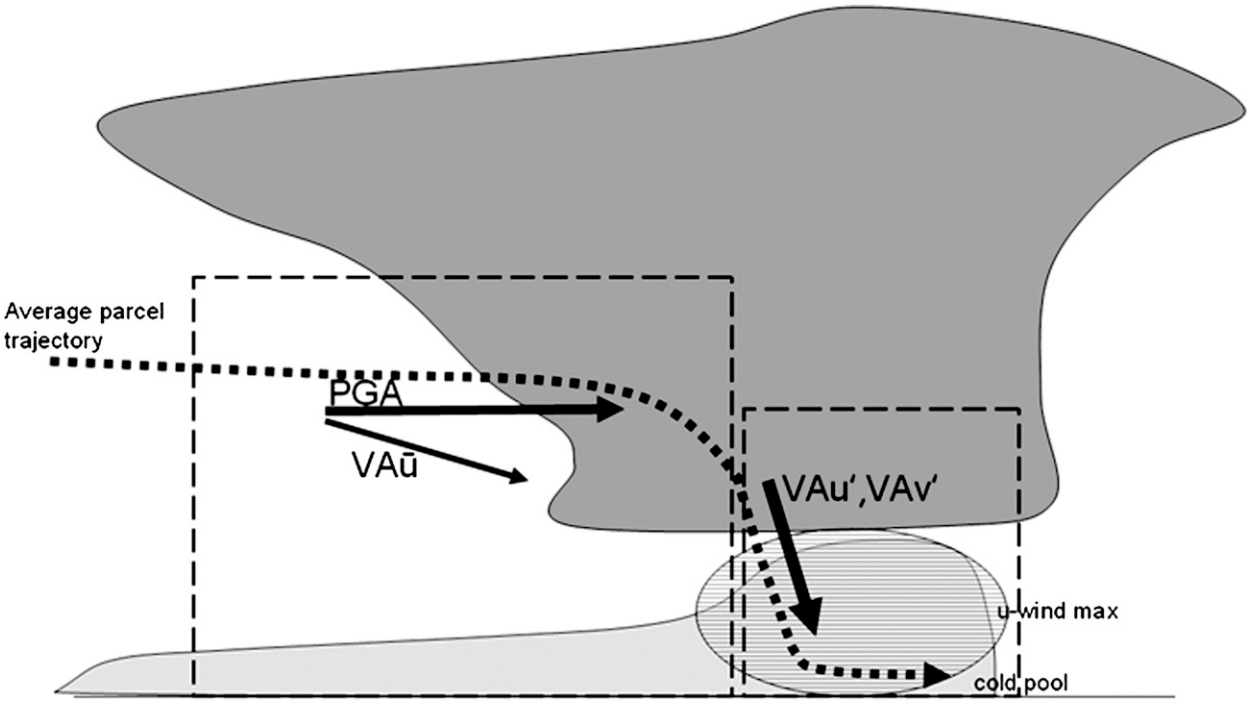

FIG. 17. Schematic of relative contributions of momentum budget terms PGA, VA processes to CMT as indicated by black arrows (thickness of arrows is an approximate indication of relative magnitude of terms, and dashed boxes show general locations of $VOL_{leading}$ and $VOL_{trailing}$).

reveals a direct connection between the RIJ and the cold pool as suggested by many past studies (e.g., Zipser 1977; Smull and Houze 1987; Lafore and Moncrieff 1989), and that in many places near the leading portion of the system, the RIJ indeed descends to the surface (or closely above). As discussed by previous studies (e.g., Newton 1950; Johns and Doswell 1992; Weisman 1992; Geerts 2001) this detail holds important implications for wind speeds experienced at the earth's surface.

While it is difficult to precisely quantify the total impact of $VA\bar{u}$ to system motion (as it is an integrated effect along the RIJ), positive $VA\bar{u}$ tendencies in the trailing stratiform region suggest that this process does contribute nonnegligibly to increasing momentum toward the leading portion of the cold pool. Furthermore, evaluating the background wind speed differences of Lagrangian budget parcels reveals that $VA\bar{u}$ may be responsible for increasing the local wind speed in the cold pool by 5–10 m s^{-1} during times of maximum parcel descent. The importance of the environmental background flow has been indicated by past studies as well; Evans and Doswell (2001) suggest that the strength of the background wind field may play an important role in both the motion of MCSs as well as the potential for severe surface wind damage. Furthermore, vertical motions and associated mass transports in the trailing stratiform region of MCSs are also shown to be important to both system dynamics and precipitation processes in studies such as Yuter and Houze (1995), Mechem et al. (2006), and Grim et al. (2009).

c. Synthesis

Figure 17 schematizes the processes described by the momentum budgets, synthesizing the main results gleaned from horizontal and vertical cross sections, parcel trajectories, and storm-following volume averages. The schematic illustrates the strength of VAu' in the fore of the system, while emphasizing the dominance of PGA and $VA\bar{u}$ in the rear of the system. While the magnitudes of latter two terms are less in $VOL_{trailing}$ than VAu' in $VOL_{leading}$, their contribution to the rear-to-front wind field in $VOL_{trailing}$ is critical, particularly the acceleration imparted by the PGA term, as noted by the Lagrangian momentum budget. The combined impact of these processes on system motion can be noted most clearly from F05 to F07, as the eastward-accelerating budget terms near the leading edge result in accelerated MCS motion (e.g., Figs. 7 and 12). The results from this analysis show that the vertical advection of accelerated perturbation winds (and to a lesser degree, the vertical advection of the ambient momentum) contributes nonnegligibly to the strength of the winds in the cold pool and the forward speed of the system.

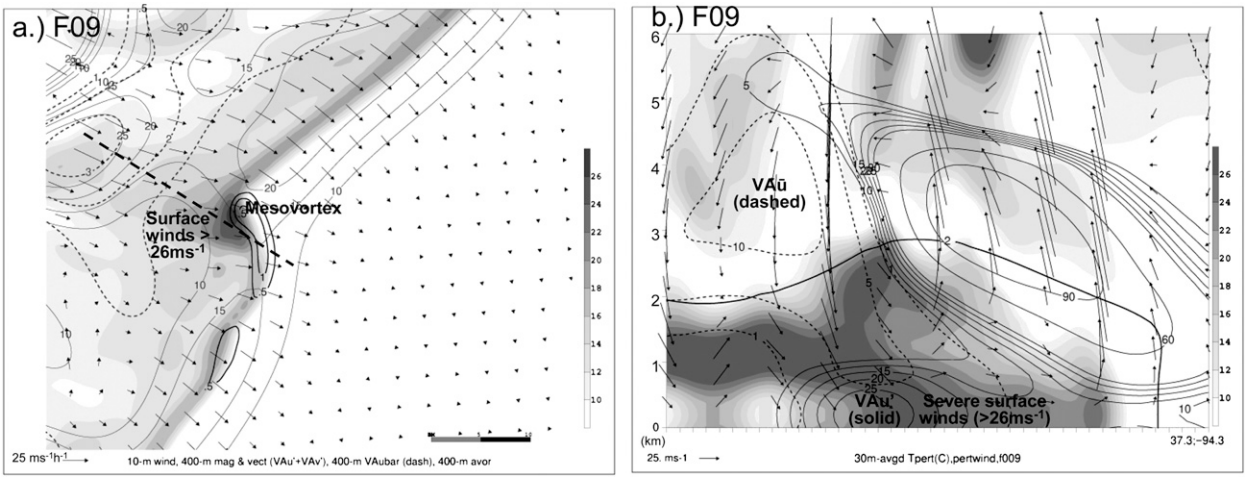

FIG. 18. (a) Magnitude of 10-m wind field (m s^{-1}, shaded), absolute vorticity (at 400 m, every 0.5×10^{-2} s^{-1}, thick black contours), $VAu' + VAv'$ (at 400 m, magnitude in thin contours every 5 m s^{-1} h^{-1} beginning at 10, vectors according to reference vector), and $VA\bar{u}$ (at 400 m, every 1 m s^{-1} h^{-1} beginning at 1, dashed contours) at F09. (b) Cross section shown by dashed line in (a), magnitude of wind (m s^{-1}, shaded), VAu' (m s^{-1} h^{-1}, solid contours), $VA\bar{u}$ (m s^{-1} h^{-1}, dashed contours), cold pool outline $T = -2$°C (thick black contour), black arrows show ground-relative flow in the x–z plane scaled as shown by reference vector in lower-left corner.

Finally, as previously discussed, this study not only seeks to quantify the contribution of CMT to MCS motion, but also to determine the specific physical process responsible for this acceleration. The results presented herein show that downward transport from aloft increases wind speeds within the cold pool and thereby accelerates the ground speed of both the cold pool and MCS itself. Thus, the change in MCS speed is due to changes in the propagative component of motion, $\mathbf{C}_P$ [i.e., hypothesis (2) listed in section 2b]. This is supported by (i) the favorable agreement and correlation found between the wind speeds in the cold pool and the speed at which the system moves (e.g., Fig. 7), (ii) the behavior of air parcels as they accelerate and then descend into the cold pool from aloft (e.g., Fig. 16), and (iii) the inability of the mean cloud-bearing wind to account for the MCS speed (Fig. 7). Therefore, the process is *not* a simple strengthening of the mean cloud-bearing-wind that results in increased advection, but rather an acceleration of the cold pool itself, and the subsequent acceleration of the system. Thus, for MCSs that are cold pool driven, the downward transport of high-momentum air from aloft increases the speed at which the entire system propagates (assuming that the pre-MCS environment continues to support convective development).

5. Conclusions and continuing work

This study demonstrates that the motion of a numerically simulated MCS is significantly impacted by the transport of horizontal momentum by vertical motions within the MCS. Momentum budgets of a simulated midlatitude MCS are computed and reveal that the vertical advection of the perturbation wind (VAu') contributes largely to the momentum field at the leading edge of the cold pool—the region in which the resulting accelerated winds drive system motion. Additionally, the momentum budgets also show that the pressure gradient acceleration (PGA) and, to a lesser degree the vertical advection of the background environmental wind ($VA\bar{u}$), contribute to the acceleration of rear-to-front momentum in the mid- to rearward portions of the storm, generating and reinforcing the perturbation flow transports into the cold pool and accelerating the MCS.

The simulation presented here illustrates a significant contribution to MCS speed from CMT: system acceleration during times of large downward transport (as shown by both the Eulerian and Lagrangian budgets) suggests a contribution to system acceleration from CMT on the order of 5–10 m s^{-1} over a period of 3–4 h (Figs. 7 and 12). While previous studies have examined CMT from alternative angles such as its role in generating severe surface winds or driving the large-scale momentum budget, the process is rarely considered in the literature as one that significantly influences the speed at which MCSs move (as opposed to buoyancy effects in the cold pool, gravity wave motion, etc.). This work demonstrates the specific role of CMT in accelerating MCS motion using trajectories, momentum fluxes, and both Eulerian and Lagrangian momentum budgets to elucidate this contribution both qualitatively and quantitatively.

The significance of the contribution of CMT to the total MCS momentum field also illustrates that the omission of this process in many operational NWP

model CP schemes is questionable, and may contribute to a negative bias in numerical forecasts of MCS motion at grid lengths where CP schemes are needed (Mahoney and Lackmann 2007). When considering the potential impact of an acceleration on the order of 5–10 m s^{-1} as noted above, over a 12- or 24-h operational forecast utilizing a CP scheme and thus neglecting this process, such a difference is clearly important. Even current ''manual'' MCS motion forecast methods [e.g., Corfidi vectors; Corfidi et al. 1996)] may benefit from a more precise inclusion of the CMT processes described herein. Finally, the impact of this process is of importance to severe weather forecasting: downward CMT in MCSs likely contributes to severe surface winds and downbursts (e.g., Johns and Hirt 1987; Vescio and Johnson 1992; Weisman 1992; Geerts 2001), and possibly tornadogenesis as well (e.g., Atkins et al. 2005). Several recent studies have discussed the combined role of mesovortices along the leading edge of the convective line and a descending RIJ in causing strong surface winds (e.g., Trapp and Weisman 2003; Wakimoto et al. 2006; Atkins and St. Laurent 2009). Such a process appears to occur in the present simulation as well, and both the VA$\overline{u}$ and VAu' processes are found to be drivers in the genesis of severe surface winds that occur in conjunction with a descending RIJ and a low-level mesovortex (Fig. 18). While the specific implications of this relationship are beyond the scope of this particular work, this is an avenue of possible future investigation.

Because of the significance that CMT holds for severe weather analysis and forecasting, further work to better understand the process is ongoing. Future work will explore how changes in large-scale environmental wind speeds impact CMT and MCS motion in general. By altering the initial background environment, we will also further distinguish the impact on MCS motion of transporting large-scale upper-level winds downward from the effect of transporting enhanced perturbation winds, and also the role of the trailing stratiform region in determining the relative importance of each. This distinction bears important consequences for successful implementation of the effect into CP schemes (e.g., in simulations in which grid spacing is large enough to necessitate a CP scheme) as perturbation winds are largely the product of subgrid-scale processes and therefore more difficult to parameterize relative to background/large-scale winds. Work is also ongoing to examine the impact of CMT on both the direction and magnitude of the low-level shear vector in order to further elucidate the role of CMT in determining the propagative component of MCS motion. Additional goals include further incorporating CMT into the MCS forecast process, both by improved treatment in existing CP schemes and also by more completely integrating CMT into conceptual models of MCS motion.

Acknowledgments. The authors gratefully acknowledge S. Trier, M. Weisman, J. Trapp, and two anonymous reviewers for insightful feedback and valuable suggestions regarding this work. Gratitude is also extended to J. Kain, M. Coniglio, S. Yuter, and A. Aiyyer for helpful discussions of this research, as well as K. Hill for an early version of the initial condition software. Support for this research was provided by National Science Foundation Grant ATM-0603760, awarded to North Carolina State University. The authors also thank NCAR and the National Science Foundation for the availability of the WRF model.

REFERENCES

Atkins, N. T., and M. St. Laurent, 2009: Bow echo mesovortices. Part I: Processes that influence their damaging potential. *Mon. Wea. Rev.,* **137,** 1497–1513.

——, C. S. Bouchard, R. W. Przybylinski, R. J. Trapp, and G. Schmocker, 2005: Damaging surface wind mechanisms within the 10 June 2003 Saint Louis bow echo during BAMEX. *Mon. Wea. Rev.,* **133,** 2275–2296.

Betts, A. K., 1986: A new convective adjustment scheme. Part I: Observational and theoretical basis. *Quart. J. Roy. Meteor. Soc.,* **112,** 677–691.

Bluestein, H. B., 1993: *Synoptic-Dynamic Meteorology in Midlatitudes*. Vol. 2, *Observations and Theory of Weather Systems,* Oxford University Press, 594 pp.

——, and M. H. Jain, 1985: Formation of mesoscale lines of precipitation: Severe squall lines in Oklahoma during the spring. *J. Atmos. Sci.,* **42,** 1711–1732.

Brandes, E. A., 1977: Flow in severe thunderstorms observed by dual-Doppler radar. *Mon. Wea. Rev.,* **105,** 113–120.

Braun, S. A., and R. A. Houze, 1997: The evolution of the 10–11 June 1985 PRE-STORM squall line: Initiation, development of rear inflow, and dissipation. *Mon. Wea. Rev.,* **125,** 478–504.

Bryan, G. H., and R. Rotunno, 2008: Gravity currents in a deep anelastic atmosphere. *J. Atmos. Sci.,* **65,** 536–556.

——, J. C. Wyngaard, and J. M. Fritsch, 2003: Resolution requirements for the simulation of deep moist convection. *Mon. Wea. Rev.,* **131,** 2394–2416.

Carr, M. T., and C. S. Bretherton, 2001: Convective momentum transport over the tropical Pacific: Budget estimates. *J. Atmos. Sci.,* **58,** 1673–1693.

Charba, J., 1974: Application of gravity current model to analysis of squall-line gust front. *Mon. Wea. Rev.,* **102,** 140–156.

Corfidi, S. F., 2003: Cold pools and MCS propagation: Forecasting the motion of downwind-developing MCSs. *Wea. Forecasting,* **18,** 997–1017.

——, J. H. Meritt, and J. M. Fritsch, 1996: Predicting the movement of mesoscale convective complexes. *Wea. Forecasting,* **11,** 41–46.

Correia, J., R. W. Arritt, and C. J. Anderson, 2008: Idealized mesoscale convective system structure and propagation using convective parameterization. *Mon. Wea. Rev.,* **136,** 2422–2442.

Engerer, N. A., D. J. Stensrud, and M. C. Coniglio, 2008: Surface characteristics of observed cold pools. *Mon. Wea. Rev.,* **136,** 4839–4849.

Evans, J. S., and C. A. Doswell, 2001: Examination of derecho environments using proximity soundings. *Wea. Forecasting,* **16,** 329–342.

Fovell, R. G., G. L. Mullendore, and S. H. Kim, 2006: Discrete propagation in numerically simulated nocturnal squall lines. *Mon. Wea. Rev.,* **134,** 3735–3752.

Fritsch, J. M., and G. S. Forbes, 2001: Mesoscale convective systems. *Severe Convective Storms, Meteor. Monogr.,* No. 50, Amer. Meteor. Soc., 323–357.

Gallus, W. A., and R. H. Johnson, 1992: The momentum budget of an intense midlatitude squall line. *J. Atmos. Sci.,* **49,** 422–450.

——, and M. Pfeifer, 2008: Intercomparison of simulations using 5 WRF microphysical schemes with dual-Polarization data for a German squall line. *Adv. Geosci.,* **16,** 109–116.

Gao, K., D.-L. Zhang, M. W. Moncrieff, and H.-R. Cho, 1990: Mesoscale momentum budget in a midlatitude squall line: A numerical case study. *Mon. Wea. Rev.,* **118,** 1011–1028.

Geerts, B., 2001: Estimating downburst-related maximum surface wind speeds by means of proximity soundings in New South Wales, Australia. *Wea. Forecasting,* **16,** 261–269.

Goff, C. R., 1976: Vertical structure of thunderstorm outflows. *Mon. Wea. Rev.,* **104,** 1429–1440.

Grell, G. A., 1993: Prognostic evaluation of assumptions used by cumulus parameterizations. *Mon. Wea. Rev.,* **121,** 764–787.

Grim, J. A., G. M. McFarquhar, R. M. Rauber, A. M. Smith, and B. F. Jewett, 2009: Microphysical and thermodynamic structure and evolution of the trailing stratiform regions of mesoscale convective systems during BAMEX. Part II: Column model simulations. *Mon. Wea. Rev.,* **137,** 1186–1205.

Grubišić, V., and M. W. Moncrieff, 2000: Parameterization of convective momentum transport in highly baroclinic conditions. *J. Atmos. Sci.,* **57,** 3035–3049.

Haertel, P. T., and R. H. Johnson, 2000: The linear dynamics of squall line mesohighs and wake lows. *J. Atmos. Sci.,* **57,** 93–107.

Han, J., and H.-L. Pan, 2006: Sensitivity of hurricane intensity forecast to convective momentum transport parameterization. *Mon. Wea. Rev.,* **134,** 664–674.

Hogan, T. F., and R. L. Pauley, 2007: The impact of convective momentum transport on tropical cyclone track forecasts using the Emanuel cumulus parameterization. *Mon. Wea. Rev.,* **135,** 1195–1207.

Hong, S. Y., Y. Noh, and J. Dudhia, 2006: A new vertical diffusion package with an explicit treatment of entrainment processes. *Mon. Wea. Rev.,* **134,** 2318–2341.

Houze, R. A., Jr., 1973: A climatological study of vertical transports by cumulus-scale convection. *J. Atmos. Sci.,* **30,** 1112–1123.

——, 2004: Mesoscale convective systems. *Rev. Geophys.,* **42,** RG4003, doi:10.1029/2004RG000150.

——, S. A. Rutledge, M. I. Biggerstaff, and B. F. Smull, 1989: Interpretation of Doppler weather radar displays in midlatitude mesoscale convective systems. *Bull. Amer. Meteor. Soc.,* **70,** 608–619.

——, B. F. Smull, and P. Dodge, 1990: Mesoscale organization of springtime rainstorms in Oklahoma. *Mon. Wea. Rev.,* **118,** 613–654.

——, S. S. Chen, D. E. Kingsmill, Y. Serra, and S. E. Yuter, 2000: Convection over the Pacific warm pool in relation to the atmospheric Kelvin–Rossby wave. *J. Atmos. Sci.,* **57,** 3058–3089.

Janjić, Z. I., 1994: The step-mountain eta coordinate model: Further developments of the convection, viscous sublayer, and turbulence closure schemes. *Mon. Wea. Rev.,* **122,** 927–945.

Jewett, B. F., and R. B. Wilhelmson, 2006: The role of forcing in cell morphology and evolution within midlatitude squall lines. *Mon. Wea. Rev.,* **134,** 3714–3734.

Johns, R. H., and W. D. Hirt, 1987: Derechos: Widespread convectively induced windstorms. *Wea. Forecasting,* **2,** 32–49.

——, and C. A. Doswell, 1992: Severe local storms forecasting. *Wea. Forecasting,* **7,** 588–612.

Kain, J. S., and J. M. Fritsch, 1993: Convective parameterization for mesoscale models: The Kain-Fritsch scheme. *The Representation of Cumulus Convection in Numerical Models, Meteor. Monogr.,* No. 46, Amer. Meteor. Soc., 165–170.

Klimowski, B. A., 1994: Initiation and development of rear inflow within the 28–29 June 1989 North Dakota mesoconvective system. *Mon. Wea. Rev.,* **122,** 765–779.

Lafore, J. P., and M. W. Moncrieff, 1989: A numerical investigation of the organization and interaction of the convective and stratiform regions of tropical squall lines. *J. Atmos. Sci.,* **46,** 521–544.

LeMone, M. A., 1983: Momentum transport by a line of cumulonimbus. *J. Atmos. Sci.,* **40,** 1815–1834.

Lynn, B. H., A. P. Khain, J. Dudhia, D. Rosenfeld, A. Pokrovsky, and A. Seifert, 2005: Spectral (bin) microphysics coupled with a mesoscale model (MM5). Part II: Simulation of a CAPE rain event with a squall line. *Mon. Wea. Rev.,* **133,** 59–71.

Mahoney, K. M., and G. M. Lackmann, 2007: The effect of upstream convection on downstream precipitation. *Wea. Forecasting,* **22,** 255–277.

Mechem, D. B., S. S. Chen, and R. A. Houze Jr., 2006: Momentum transport processes in the stratiform regions of mesoscale convective systems over the western Pacific warm pool. *Quart. J. Roy. Meteor. Soc.,* **132,** 709–736.

Moncrieff, M. W., and C. Liu, 2006: Representing convective organization in prediction models by a hybrid strategy. *J. Atmos. Sci.,* **63,** 3404–3420.

Morrison, H., G. Thompson, and V. Tatarskii, 2009: Impact of cloud microphysics on the development of trailing stratiform precipitation in a simulated squall line: Comparison of one- and two-moment schemes. *Mon. Wea. Rev.,* **137,** 991–1007.

Newton, C. W., 1950: Structure and mechanisms of the prefrontal squall line. *J. Meteor.,* **7,** 210–222.

——, and H. R. Newton, 1959: Dynamical interactions between large convective clouds and environments with vertical shear. *J. Meteor.,* **16,** 483–496.

Nicholls, M. E., R. H. Johnson, and W. R. Cotton, 1988: The sensitivity of two-dimensional simulations of tropical squall lines to environmental profiles. *J. Atmos. Sci.,* **45,** 3625–3649.

Pandya, R. E., and D. R. Durran, 1996: The influence of convectively generated thermal forcing on the mesoscale circulation around squall lines. *J. Atmos. Sci.,* **53,** 2924–2951.

Parker, M. D., and R. H. Johnson, 2004: Structures and dynamics of quasi-2D mesoscale convective systems. *J. Atmos. Sci.,* **61,** 545–567.

Richardson, Y. P., K. K. Droegemeier, and R. P. Davies-Jones, 2007: The influence of horizontal environmental variability on numerically simulated convective storms. Part I: Variations in vertical shear. *Mon. Wea. Rev.,* **135,** 3429–3455.

Rotunno, R., J. B. Klemp, and M. L. Weisman, 1988: A theory for strong, long-lived squall lines. *J. Atmos. Sci.,* **45,** 463–485.

Sanders, F., and K. A. Emanuel, 1977: The momentum budget and temporal evolution of a mesoscale convective system. *J. Atmos. Sci.,* **34,** 322–330.

Skamarock, W. C., M. L. Weisman, and J. B. Klemp, 1994: Three-dimensional evolution of simulated long-lived squall lines. *J. Atmos. Sci.,* **51,** 2563–2584.

——, J. B. Klemp, J. Dudhia, D. O. Gill, D. M. Barker, W. Wang, and J. G. Powers, 2007: A description of the advanced research WRF version 2. NCAR Tech. Note NCAR/TN-475+STR, 125 pp.

Smull, B. F., and R. A. Houze Jr., 1987: Rear inflow in squall lines with trailing stratiform precipitation. *Mon. Wea. Rev.,* **115,** 2869–2889.

Srivastava, R., 1987: A model of intense downdrafts driven by the melting and evaporation of precipitation. *J. Atmos. Sci.,* **44,** 1752–1774.

Trapp, R. J., and M. L. Weisman, 2003: Low-level mesovortices within squall lines and bow echoes. Part II: Their genesis and implications. *Mon. Wea. Rev.,* **131,** 2804–2823.

Trier, S. B., M. A. LeMone, and W. C. Skamarock, 1998: Effect of three-dimensional structure on the stormwide horizontal accelerations and momentum budget of a simulated squall line. *Mon. Wea. Rev.,* **126,** 2580–2598.

——, C. A. Davis, D. A. Ahijevych, M. L. Weisman, and G. H. Bryan, 2006: Mechanisms supporting long-lived episodes of propagating nocturnal convection within a 7-day WRF model simulation. *J. Atmos. Sci.,* **63,** 2437–2461.

van den Broeke, M. S., D. M. Schultz, R. H. Johns, J. S. Evans, and J. E. Hales, 2005: Cloud-to-ground lightning production in strongly forced, low-instability convective lines associated with damaging wind. *Wea. Forecasting,* **20,** 517–530.

Vescio, M. D., and R. H. Johnson, 1992: The surface-wind response to transient mesoscale pressure fields associated with squall lines. *Mon. Wea. Rev.,* **120,** 1837–1850.

Wakimoto, R. M., H. V. Murphey, C. A. Davis, and N. T. Atkins, 2006: High winds generated by bow echoes. Part II: The relationship between the mesovortices and damaging straight-line winds. *Mon. Wea. Rev.,* **134,** 2813–2829.

Weisman, M. L., 1992: The role of convectively generated rear-inflow jets in the evolution of long-lived mesoconvective systems. *J. Atmos. Sci.,* **49,** 1826–1847.

——, 1993: The genesis of severe, long-lived bow echoes. *J. Atmos. Sci.,* **50,** 645–670.

——, and J. B. Klemp, 1982: The dependence of numerically simulated convective storms on vertical wind shear and buoyancy. *Mon. Wea. Rev.,* **110,** 504–520.

——, and ——, 1986: Characteristics of isolated convective storms. *Mesoscale Meteorology and Forecasting,* P. S. Ray, Ed., Amer. Meteor. Soc., 331–357.

——, W. C. Skamarock, and J. B. Klemp, 1997: The resolution dependence of explicitly modeled convective systems. *Mon. Wea. Rev.,* **125,** 527–548.

Wu, X., and M. Yanai, 1994: Effects of vertical wind shear on the cumulus transport of momentum: Observations and parameterization. *J. Atmos. Sci.,* **51,** 1640–1660.

——, L. Deng, X. Song, and G. J. Zhang, 2007: Coupling of convective momentum transport with convective heating in global climate simulations. *J. Atmos. Sci.,* **64,** 1334–1349.

Yang, M.-J., and R. A. Houze Jr., 1996: Momentum budget of a squall line with trailing stratiform precipitation: Calculations with a high-resolution numerical model. *J. Atmos. Sci.,* **53,** 3629–3652.

Yuter, S. E., and R. A. Houze Jr., 1995: Three-dimensional kinematic and microphysical evolution of Florida cumulonimbus. Part III: Vertical mass transport, mass divergence, and synthesis. *Mon. Wea. Rev.,* **123,** 1964–1983.

Zhang, D.-L., K. Gao, and D. B. Parsons, 1989: Numerical simulation of an intense squall line during 10–11 June 1985 PRE-STORM. Part I: Model verification. *Mon. Wea. Rev.,* **117,** 960–994.

Zhang, Q. H., K. H. Lau, Y. H. Kuo, and S. J. Chen, 2003: A numerical study of a mesoscale convective system over the Taiwan Strait. *Mon. Wea. Rev.,* **131,** 1150–1170.

Zipser, E., 1977: Mesoscale and convective–scale downdrafts as distinct components of squall-line structure. *Mon. Wea. Rev.,* **105,** 1568–1589.